Nanostructured Origami^{TM}: Folding Thin Films out of the Plane of a Silicon Wafer with Highly Stressed Chromium Hinges

by
William Jay Arora
S.B., Electrical Engineering,
Massachusetts Institute of Technology (2003)

Submitted to the
Department of Electrical Engineering and Computer Science
in partial fulfillment of the requirements for the degree of
Master of Engineering in Electrical Engineering
at the
MASSACHUSETTS INSTITUTE OF TECHNOLOGY
June 2005

Author .....
Department of Electrical Engineering and Computer Science
May 19, 2005

Certified by .....
George Barbastathis
Assistant Professor of Mechanical Engineering
Thesis Supervisor

Certified by .....
Henry I. Smith
Professor of Electrical Engineering
Thesis Supervisor

Accepted by ..
Arthur C. Smith
Chairman, Department Committee on Graduate Students

Nanostructured Origami^{TM}: Folding Thin Films out of the Plane of a Silicon Wafer with Highly Stressed Chromium Hinges

by

William Jay Arora

Submitted to the
Department of Electrical Engineering and Computer Science
on May 19, 2005, in partial fulfillment of the
requirements for the degree of
Master of Engineering in Electrical Engineering

Abstract

This thesis addresses the construction of complex three-dimensional (3-D) nanostructures using only 2-D, planar nano-fabrication techniques. In the state of the art, multiple 2-D layers are fabricated in series, each directly on top of the previous. The method advocated here is Nanostructured Origami, in which multiple adjacent 2-D layers are fabricated in parallel and are then folded into the desired 3-D configuration using the appropriate folding sequence. This thesis focuses on folding actuation for this method using the residual tensile stress in vacuum-evaporated chromium to fold silicon nitride membranes. Our results conclusively demonstrate the ability to pattern these membranes with nano-scale features and then controllably fold them into a predetermined 3-D configuration. Future work will refine the fabrication procedure for large-scale manufacturing and address alignment and latching of the folded membranes.

Thesis Supervisor: George Barbastathis
Title: Assistant Professor of Mechanical Engineering

Thesis Supervisor: Henry I. Smith
Title: Professor of Electrical Engineering

Foreword

I have had the extraordinary privilege of conducting my graduate research under the supervision of Professor Henry Smith, a living legend in the field of nanotechnology, and Professor George Barabastathis, a young genius in the field of optics. The original concept of Nanostructured Origami was Hank's, and George was quick to foresee applications in the area of 3-D optical devices. I am thankful to Hank for the complete freedom he gave me to experiment in the lab, with just the right advice to make sure my research stayed on track. Working in the Nanostructures Lab has been a joy and has convinced me to pursue a research career in nanotechnology. I am thankful to George for the detailed discussions we had about my research in which his insightful feedback always made me rethink my logic and consider new ideas. His encouragement when my experiments repeatedly failed is what kept me going until that thrilling day in January when "it worked." He set the bar higher than I ever would have and somehow made sure I cleared it. My advisors' academic support for me has been unwaveringly strong even through my mistakes and for this I am in their debt. Their guidance has not only assisted my research but has helped me mature personally and professionally.

This thesis presents our first attempts at Nanostructured Origami. The fabrication process is rudimentary and the results, while eye-catching, are not yet useful. However, I am confident that with a few more years of work we will achieve something functional and spectacular.

Many people helped me in all aspects of this project. In particular, this thesis would not have been possible without the laboratory assistance of Jim Daley. I am extremely thankful for his advice and help which he provided whenever I asked for it and often without my asking. His genuine care for my research (and all of the other students' research) along with his daily good humor gave color to the otherwise monochromatic clean room. Also, many of my colleagues in the Nanostructures Lab and 3-D Optics Lab communities went out of their way to help me, notably Chih-Hao Chang, Ion Bita, Kurt Broderick, Tony Nichol, Hyun Jin In, Tim Savas, Paul

Stellman, Nader Shaar, Vikas Anant, Mark Mondol, Chris Dames, Fernando Castano, Mike Walsh, Feng Zhang, Karl Berggren, Mirielle Akilian, Minghao Qi, Tymon Barwicz, Amil Patel, David Chao, Jim Carter, Nicole Hanafin and Cindy Lewis. To list all of their contributions would take far too long.

This thesis is dedicated to my parents and to God, whose overflowing love and generous support have carried me through twenty-four years.

W. J. Arora

Cambridge, Massachusetts
May 2005

Contents

List of Figures

List of Tables

Chapter 1

Introduction

The purpose of this investigation was to characterize, test and evaluate the concept of using stressed metal hinges to fold nano-patterned thin films into 3-D configurations on a silicon wafer. The concept of folding nano-patterned membranes into 3-D shapes is referred to as Nanostructured Origami because of the similarity to the Japanese paper-art of origami in which 2-D surfaces are folded into volumetric shapes. In Nanostructured Origami the surfaces are first nano-patterned with functional devices and the folding is not manual but self-actuated.

Presently there are no effective and general ways to realize 3-D nanostructures; our best efforts involve stacking multiple 2-D layers in series, each directly on top of the previous. This approach is a result of the current nanofabrication tools which operate only on planar substrates. Therefore the ultimate goal of Nanostructured Origami is to become a tool by which we can fabricate complex 3-D nanostructures. The following sections elaborate on the reasoning behind the folding method, provide motivational examples for the work, describe the major engineering requirements of the method, summarize the prior art of membrane folding, explain why stress-actuated folding was investigated in this thesis, and present an overview of the contents of this thesis.

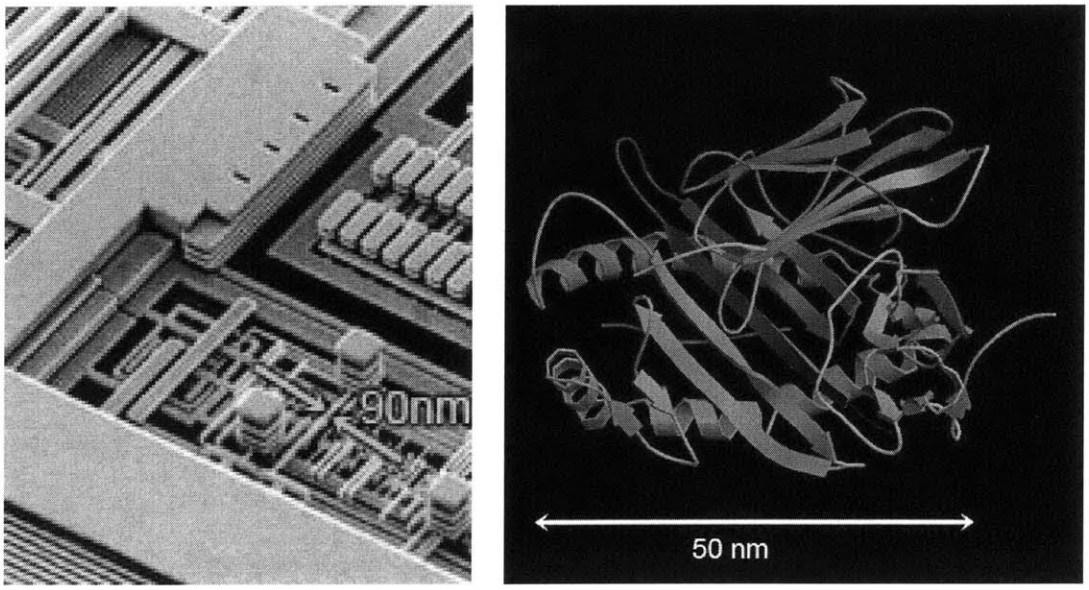

(a) (b)

Figure 1-1: (a) Isometric view of an integrated circuit © IBM 2005. (b) Computer generated model of protein folding. The protein is a component of the major histocompatibility complex (immune system). Key: Light blue = carbon, dark blue = nitrogen, red = oxygen, yellow = sulfur. Arrows depict folding trajectories.

1.1 3-D Nano-Manufacturing by Nature and by Man

Motivation for this project comes from contrasting our current efforts at 3-D nano-manufacturing with the way biological cells build 3-D nanostructures. We are building precision lithography tools that can pattern features down to 10nm, a limit that is continually shrinking. However, these tools all operate on planar substrates which confines our efforts at building in 3-D to stacking layers. Fig. 1-1a illustrates this concept by showing a complicated integrated circuit with many layers that have been stacked upon one another.

In stark contrast, the cells in our body manufacture 3-D nanostructures such as proteins by folding. Fig. 1-1b shows how proteins, the major building block of biological systems, are formed by the spontaneous folding of linear precursors. In addition, the folded molecules of the protein may terminate in a way that allows

Figure 1-2: Folding a pre-patterned membrane into a 3-D configuration will maximize the possible interconnections and make best use of available space.

them to preferentially bind to other proteins and self-assemble in 3-D.

The key difference between these two methods is folding versus stacking. Therefore, the crux of Nanostructured Origami is membrane folding. Pre-patterning membranes prior to folding will result in 3-D configurations of high information density. A schematic example of this is shown in Fig. 1-2.

1.2 Applications of Nanostructured Origami

Presented below are two examples of actual devices that are nearly impossible to fabricate with planar stacking and may be much easier to fabricate with origami. The first is a 3-D photonic crystal (acting as an optical waveguide). Over the recent years, many have tried to build this structure but with moderate success due to lithography and other processing limitations. Fig. 1-3 shows a seven-layer photonic crystal fabricated with layer-by-layer stacking [1] and contrasts that approach with the folding approach.

A multilayer Fresnel zone plate is another device that could be best fabricated with origami. The structure acts as a focusing lens and would have immense value in nanolithography applications, particularly zone-plate-array-lithography [2,3]. The structure of a 3-D zone plate fabricated by folding is illustrated in Fig. 1-4.

In both of these applications, phase alignment of the folded layers is crucial and

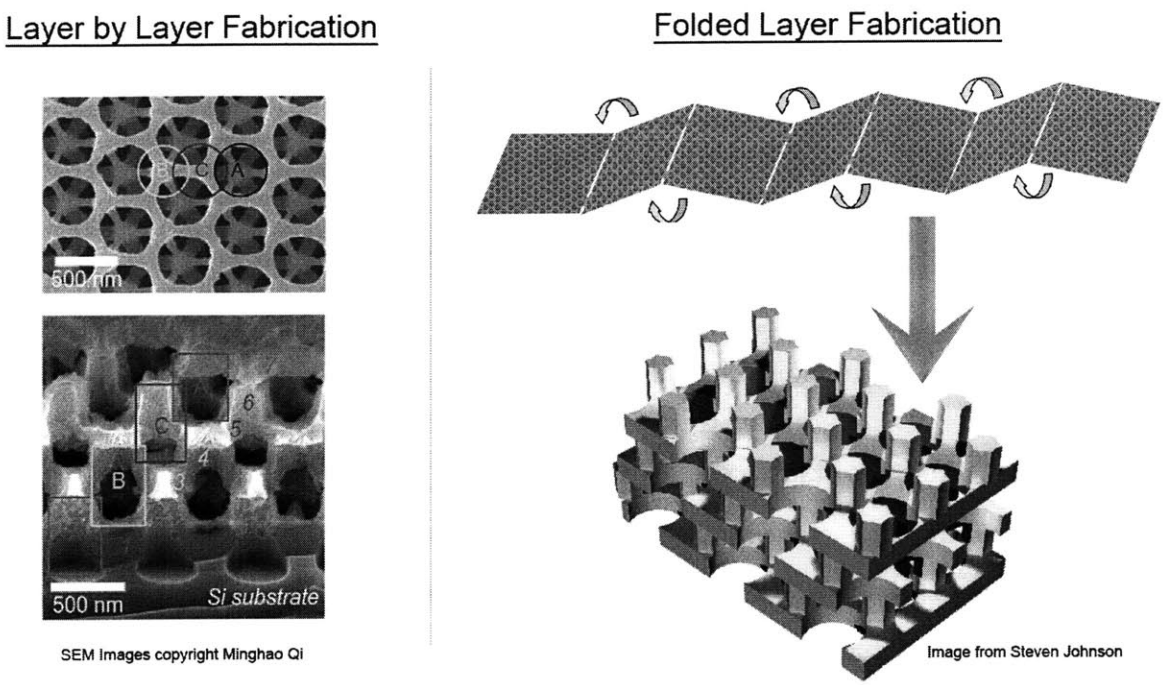

Figure 1-3: A 3-D photonic crystal fabricated in two ways; folding is a much simpler option.

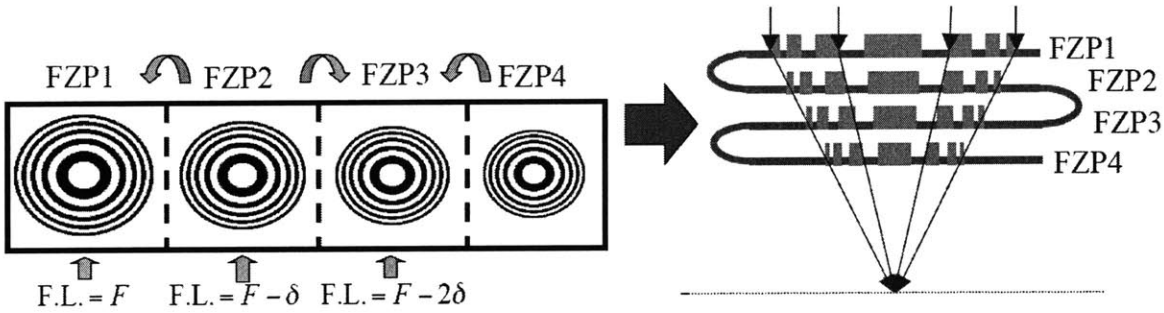

Figure 1-4: Schematic of a multilayer Fresnel zone plate (FZP) showing the folding sequence and the design and spacing of each layer.

must be less than a fraction of the operating wavelength. Depending on the particular device and wavelength used, this may be approximately 50nm. In the layer stacking fabrication approach, alignment is usually performed by viewing alignment marks on the lower layer. Optical overlay alignment has been demonstrated to less than 3nm [4] which far exceeds the alignment requirement. However, achieving such fine alignment is a slow and tedious process; furthermore, it becomes extremely complicated when more than two layers need to be aligned. The folding fabrication approach provides more options for alignment because patterned alignment features will naturally interact when they are folded together. This creates the potential for self-aligning structures. Several alignment schemes for membrane folding are discussed in Section 1.3.

Nanostructured Origami will have applications in areas other than photonics. It should be possible to create 3-D integrated circuits (ICs) which would reduce the average interconnect length between transistors and increase the overall computing density. Micro-opto-electro-mechanical systems (MOEMS) devices that are currently planar surface micro-machined will be folded into novel 3-D configurations. Bio-chemical devices will be integrated into the above devices via folding. It should be emphasized that we are developing Nanostructured Origami as a 3-D nano-manufacturing platform and these are only a few of the possible applications; the rest are waiting to be discovered.

1.3 Engineering Requirements of Nanostructured Origami

In order for Nanostructured Origami to become a useful tool, it must satisfy the following requirements. They are presented along with general ideas that may be solutions:

1. Be able to fold in and out of plane to create multilayered devices
    - Many methods for achieving this are discussed in Section 1.4

2. Be able to sequence folds in time to create complex 3-D shapes

    - Etch holes may be used to control where the release starts and finishes
    - Electrodes may be patterned to electrically control the release or folding
    - Chemical (for example, doping) gradients may be defined in the release material to alter its etch rate
    - Folding may be actuated by breaking sacrificial tabs with laser etching

3. Self-actuate or actuate without manual external manipulation

    - To self-actuate, the membranes need some stored potential energy. (For example, strain energy, chemical energy or surface tension.)
    - To actuate in an automated fashion, the membranes may have individual connections to energy sources (for example, electrical wires) or may react to an applied external field (for example, a magnetic field)

4. Fold accurately, align and latch into place

    - Mechanical stops may be used to force the folded membrane into position
    - Nano-magnets may align membranes through inherent magnetic attraction
    - Adhesive forces may be created by chemical bonding or stiction

This thesis examines the use of patterned stress areas to create out of plane folds. Future work will address the remaining requirements.

1.4 Membrane Folding Methods

Within the last decade, researchers have begun looking for ways to build 3-D structures on silicon and many methods have been investigated. Table 1.1 presents a summary of each and compares them based on the engineering requirements of Nanostructured Origami (outlined in Section 1.3).

Table 1.1: Comparison of known membrane folding methods.

od	Description	Fold Size Scale	Fold Accuracy	Self-Assembling / Sequencing
ed r	The difference in planar stress between two deposited thin films causes a bending moment that curls the bilayer structure.	10-50μm	Stress variations vary the fold angle within 10%	Each hinge has its own energy and actuates up lease. Selective etchin lease) is required to sequence the folding.
tic and ostatic 6]	The membranes are patterned with magnetic material or current-carrying wires that will cause a folding force when an external magnetic field is applied.	5-50μm	Can be controlled very precisely by rotating the applied magnetic field.	Membranes will only ass with applied magnetic fie dividual hinges may be vated sequentially by ap current.
ned 0]	Mechanical hinges are fabricated with MEMS surface micromachining techniques.	10-100μm	Fold angles are well controlled by mechanical stops and latches.	Membranes are folded ally with micro-probes. sequencing must be man
e n	Pads of solder are patterned between two membranes, melted, and allowed to resolidify. The surface tension of the liquid state causes the free membrane to fold up.	20-100μm	The fold angle varies within 10% because the melting step is hard to control.	Devices self-assemble heating and cooling. heating must be use time-sequence the foldin
nide	V-grooves are formed in a silicon membrane and filled with polyimide. Upon heating, the polyimide shrinks and bends the membrane.	100-200μm	Small angle folds are well controlled but large angle folds (> 90°) vary because 5-6 grooves are necessary and the error is cumulative.	The devices are self-asse by heating. Local heatin be used to time-sequen folding.

Although they all hold promise, this study focuses on stress-induced folding because the fabrication is the simplest and the hinges self-actuate upon release without any external manipulation.

Large internal stresses in thin film vacuum-deposited metals have been observed before [23–30]. These films tend to curl into tubes with radii on the order of microns due to their internal stress [9, 10]. This effect has been generally undesirable in nanotechnology research, and a lot of work has focused on minimizing the internal stress of deposited thin films by changing the deposition parameters [31]. However, this project seeks to maximize and control the stress in order to reliably fold thin films into predictable 3-D configurations on a silicon wafer.

In 2004, Tokuda [7] was the first to demonstrate stress-actuated folding of thin films on silicon.[1] In their approach, stress is created between layers of epitaxially grown Si and SiGe due to the crystal lattice mismatch between the two layers. When this structure is released from the silicon wafer, it curls predictably and it is possible to fold a thin Si/SiGe/Si membrane. There are two advantages to this technique: first, the strain between the Si and SiGe crystalline lattices is very large, almost 3%. Second, epitaxial growth allows for precise film thickness control and a perfect crystal lattice. The main disadvantage of this technique is that randomly formed lattice dislocations at the Si/SiGe interface reduce most of the stress [7], making it difficult to keep constant. Additionally, the epitaxial growth process is slow, expensive and can only be done on top of an existing crystalline surface.

The goal of this thesis is to demonstrate controllable membrane folding using electron-beam evaporated metal. An additional goal is to demonstrate that the membranes can be nano-patterned prior to folding.

1.5 Overview of Thesis

This thesis discusses the modeling of, materials used in, and fabrication procedure of stress-actuated folding to achieve folded 3-D nanostructures. Chapter 2 describes the

[1] Stress-actuated folding was first demonstrated on GaAs substrates in 2001 [32].

stress-actuated folding concept in detail and presents an analytical model of bilayer thin film curling. Chapter 3 explains in detail how residual stress evolves in evaporated metal. It explains why we chose to work with chromium in this thesis, and presents experimental measurements of the stress obtained in chromium films evaporated in the MIT Nanostructures Lab (NSL). Chapter 4 presents experimental results that validate the concept of stress-actuated folding. In particular, we prove conclusively that the membranes can be nano-patterned and then folded. Fabrication problems, solutions and overall process improvements are discussed as well. The thesis concludes in Chapter 5 with a summary and analysis of the work as well as experiments planned for future stages of this research.

Chapter 2

Analytical Model of Stress-Actuated Folding

This chapter presents an analytical model of the stress-actuated folding mechanism. The purpose of the model is to understand the physical principles involved and to provide a good approximation of the observed experimental results. The model can then be used to optimize the folding process by calculating experimental parameters that will minimize the radius of the folds. An estimate of the folding radius also allows one to calculate the length of the chromium hinge necessary to fold to a desired angle; this was particularly useful in the experiments of Chapter 4.

2.1 Model Definition and Description

Fig. 2-1 illustrates the stress-actuated folding process. The system consists of three layers; a sacrificial layer, a structural layer and a stress layer. The sacrificial layer is a removable base on which the structural and stress layers can be fabricated. The geometry of the sacrificial layer also determines which part of the structural layer remains attached to the substrate and which part is allowed to fold. In Fig. 2-1, the sacrificial layer geometry causes the fixed boundary condition at $x = 0$. The structural layer is assumed to be conformal to the underlying substrate and sacrificial layer. It is also assumed to have no residual stresses. The stress layer is patterned

with rectangular geometry as shown (length = l, width = b) and this area is referred to as the hinge. It is assumed to have an x-z plane stress that is uniform throughout its thickness. Although ideally the stress layer would only have uniaxial stress in the x direction, there is no known way to fabricate a layer with uniaxial stress. Therefore in this model (and in experiment), we rely on the fixed boundary and rectangular geometry ($b > 2 \cdot l$) to force the folding about the z axis. Physically, the reason why the hinge curls is because the stress is not constant through the thickness (it is zero in the structural layer and finite in the stress layer); this creates an out-of-plane bending moment.

2.2 Mathematical Analysis of the Stress-Actuated Folding Model

The following variables are assigned to the system shown in Fig. 2-1:

$$\begin{aligned} t_i &\quad , \quad \text{thickness of layer } i \\ E_i &\quad , \quad \text{elastic modulus of layer } i \\ \nu_i &\quad , \quad \text{poisson ratio of layer } i \\ \sigma_i(y) &\quad , \quad \text{stress distribution in layer } i \\ \varepsilon_i(y) &\quad , \quad \text{strain distribution in layer } i \end{aligned}$$

In the post-release picture of Fig. 2-1, the structure is in static equilibrium. The equilibrium condition results in two equations,

$$0 = F = b \cdot \int_{-t_1}^{t_2} \sigma(y)\,\mathrm{d}y \tag{2.1}$$

$$0 = M = b \cdot \int_{-t_1}^{t_2} y \cdot \sigma(y)\,\mathrm{d}y \tag{2.2}$$

The total force and total bending moment equal zero. First we will calculate the forces in the system, all of which arise from stresses. There is an initial stress in layer

2 and a stress gradient from the bending in both layers. This is illustrated in Fig. 2-2. Our assumption of initial uniform plane stress means that

$$\hat{x} \cdot \sigma_i(y) = \hat{z} \cdot \sigma_i(y)\,, \tag{2.3}$$

$$\hat{y} \cdot \sigma_i(y) = 0 \tag{2.4}$$

and our assumption that the structure only bends around the z axis means

$$\hat{z} \cdot \varepsilon_i(y) = 0\,. \tag{2.5}$$

Hooke's law[1] states that strain in the x and z axes is

$$\hat{x} \cdot \varepsilon_i(y) = \frac{\hat{x} \cdot \sigma_i(y)}{E_i} - \nu \cdot \frac{\hat{z} \cdot \sigma_i(y)}{E_i}\,, \tag{2.6}$$

$$\hat{z} \cdot \varepsilon_i(y) = \frac{\hat{z} \cdot \sigma_i(y)}{E_i} - \nu \cdot \frac{\hat{x} \cdot \sigma_i(y)}{E_i}\,. \tag{2.7}$$

Solving Eqs. 2.3 - 2.7 together we obtain

$$\hat{x} \cdot \sigma_i(y) = \frac{E_i}{1-\nu^2}\,\hat{x} \cdot \varepsilon_i(y)\,,$$

and we will define the plate modulus E_i' as

$$E_i' = \frac{E_i}{1-\nu^2}\,. \tag{2.8}$$

We now apply our initial condition assumption that $\sigma_1(y) = 0$ and $\sigma_2(y) = C$, where C is a value taken from experiment of the residual stress in the evaporated metal film.

The bending stress shown in Fig. 2-2b is expressed as

$$\hat{x} \cdot \sigma_i(y) = (A + ky) \cdot E_i' \tag{2.9}$$

[1]Hooke's law assumes that both films behave perfectly elastically. This assumption is analyzed in Section 2.5.

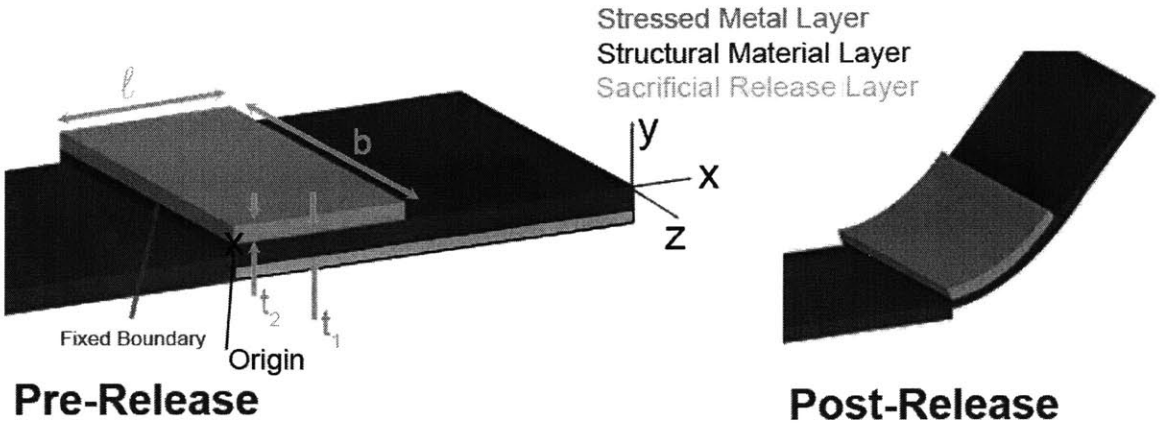

Figure 2-1: Schematic diagram of stress-actuated folding. For the purposes of mathematical modeling in Section 2.2, the origin is located at the point shown. The substrate is underneath the entire thin film stack. The structural layer is referred to as layer 1 and the stress layer is referred to as layer 2.

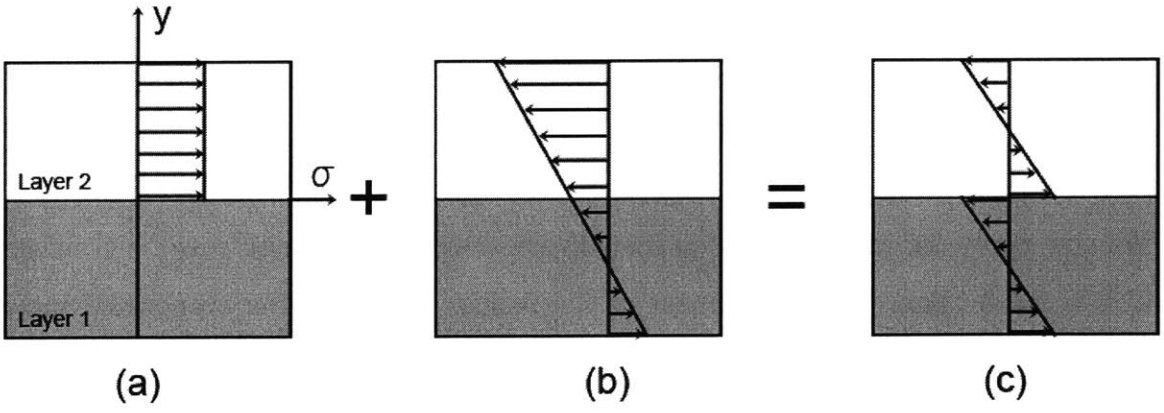

Figure 2-2: Stress distribution through the x-y cross-section of the hinge area. (a) Tensile stress in stress layer. (b) Stress generated from bending (bending not shown). (c) Total stress distribution.

where k is the curvature and A is a constant term. This is a standard result from beam bending theory. We have written equations for all of the stresses in the problem and they are all x-directed. Therefore, the problem is one-dimensional and $\hat{x}$ components are assumed. Furthermore, the subscript i is dropped and it is understood that when $y < 0$ we are referring to a function in layer 1 and when $y > 0$ we are referring to a function in layer 2. The sum of the initial and bending stresses is the total stress. In the simplified notation,

$$\sigma(y) = E'(y) \cdot (A + ky) + C\,. \tag{2.10}$$

Substituting this expression into Eqs. 2.1 and 2.2 and solving simultaneously yields an expression for the bending radius:

$$\rho = \frac{1}{k} = \frac{E_1'^2 t_1^4 + E_2'^2 t_2^4 + 2E_1' E_2' t_1 t_2 \cdot (2t_1^2 + 3t_1 t_2)}{6E_1' E_2' t_1 t_2 (t_1 + t_2) \cdot (C/E_2')}\,. \tag{2.11}$$

2.3 Applying the Mathematical Analysis to Optimize Stress-Actuated Folding

We are interested in minimizing the radius of curvature to achieve the smallest possible fold. Eq. 2.11 has five variables: t_1, t_2, E_1', E_2' and C. In our experiment, three of these variables are fixed: E_1' and E_2' are determined by the materials chosen for the structural and stress layers and C is determined by the deposition of the stress layer. Thus, for a given structural layer thickness t_1, we can plot the curvature radius as a function of the stress layer thickness t_2. To generate useful plots, we will use parameters from realistic material choices. The structural layer may be low-pressure chemical-vapor deposition (LPCVD) silicon nitride or LPCVD polysilicon.[2] The stressed metal layer may be evaporated chromium (Cr) or tungsten (W).[3] Material properties of thin films differ from their bulk properties and are dependent

[2]Discussed in Section 2.5 and Chapter 4.
[3]Discussed in Chapter 3.

Table 2.1: Estimates of the Material Properties of Thin Films Useful for Nanostructured Origami.

	LPCVD $Si_{1.0}N_{1.1}$		**LPCVD poly-Si**		**Evap. W**		**Evap. Cr**	
Elastic modulus (GPa)	300	[33]	175	[33]	350	[25]	140	[34]
Poisson ratio	0.28	[33]	0.25	[33]	0.28	[35]	0.21	[34]
Plate modulus (GPa)	326		186		380		146	
Yield strength (GPa)	9	[33]	3	[33]	1.8	[25]	0.16	[25]
Thermal expansion coefficient (x $10^{-5}\,°C^{-1}$)	3	[33]	0.42	[33]	0.43	[25]	1.6	[25]

upon the deposition method, deposition parameters, and geometry of the film. Table 2.1 provides estimates of the mechanical properties of these films taken from the literature.

In our experiment we used silicon nitride as the structural layer and chromium as the stress layer. To gain insight into the curvature formula (Eq. 2.11), the bending radius is plotted as a function of chromium layer thickness for 200nm thick silicon nitride. The following plot assumes the appropriate material parameters listed in Table 2.1 and a residual stress value of $C = 2$GPa. Clearly, it is possible to minimize

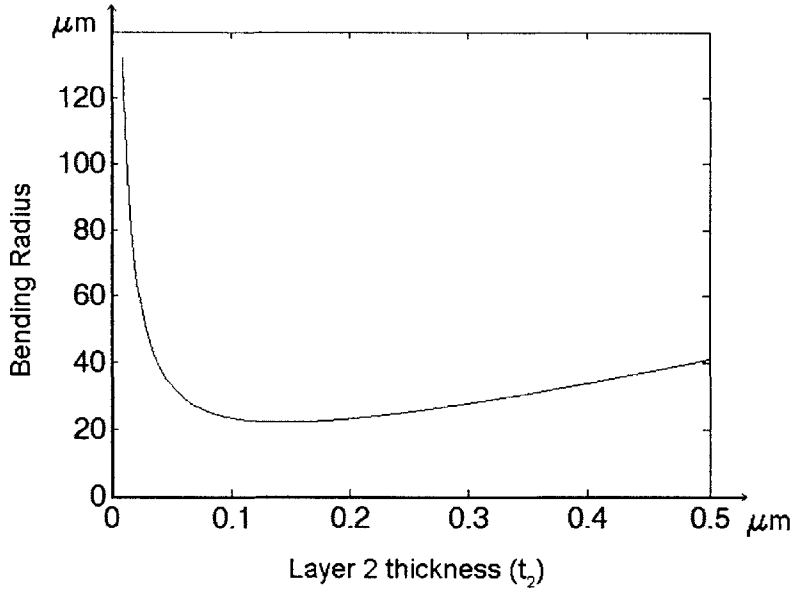

Figure 2-3: Plot of the bending radius as a function of the stress layer thickness using Eq. 2.11.

the bending radius by controlling the thickness of the stress layer. As the stress layer

thickness approaches the two limits ($t_2 \rightarrow 0$ and $t_2 \rightarrow \infty$), the radius approaches ∞. In the limit as $t_1 \rightarrow 0$, this is understood because the y-z cross-sectional area $b \cdot t_1$ is so small that there is very little force to create a bending moment. In the limit as $t_1 \rightarrow \infty$, this is understood because the structural layer thickness is almost negligible compared to the stress layer so instead of bending, the bilayer shrinks elastically within the x-z plane. The minimum radius is located between the two limits at the point where the bending moment generated by the stress layer is maximized. Mathematically, this point can be calculated by minimizing Eq. 2.11 with respect to t_2. Then, the stress layer thickness needed to minimize the radius is:

$$t_2 = t_1 \cdot \left(\frac{E_\alpha}{2E_2'} + \frac{E_2'}{2E_\alpha} - \frac{1}{2}\right) \quad \text{, where} \tag{2.12}$$

$$E_\alpha = \left[-E_2' + 2E_1' + 2 \cdot (-E_1'(E_2' - E_1'))^{1/2} \cdot E_2'^{\,2}\right]^{1/3}$$

Eq. 2.12 shows that the optimum t_2 scales linearly with t_1 but has nonlinear dependencies on E_1' and E_2'. For E_1' and E_2' = [100,400] (a realistic range of values), the optimum t_2 will range from $\frac{t_1}{4}$ to t_1. When $E_1' = E_2'$, the optimum $t_2 = \frac{t_1}{2}$.

Although E_1' and E_2' are not variable in the experiment, it is interesting to understand how they affect the bending radius. Fig. 2-4 plots the minimum obtainable radius (using the optimum t_2 as given by Eq. 2.12) as a function of E_1' and E_2'. The dominating trend is that the bending radius is proportional to E_1'/E_2'. Physically this means that the radius will be smallest when the structural layer is more compliant than the stress layer. We note that if two materials can be deposited with similar residual stress, the one with a higher elastic modulus will produce a smaller fold. However, this plot assumes a fixed strain in the stress layer which is not the case in reality. The strain depends on the material used. As an example of how this plot can be misleading, consider a stress layer made of SU-8 photoresist. Its plate modulus is 5GPa and its strain (after baking) is 7%. Even though it strains more than chromium it has a very low elastic modulus and one would not expect it to produce a small bending radius. Surprisingly though, a minimum radius of 10μm is obtained when t_2 =

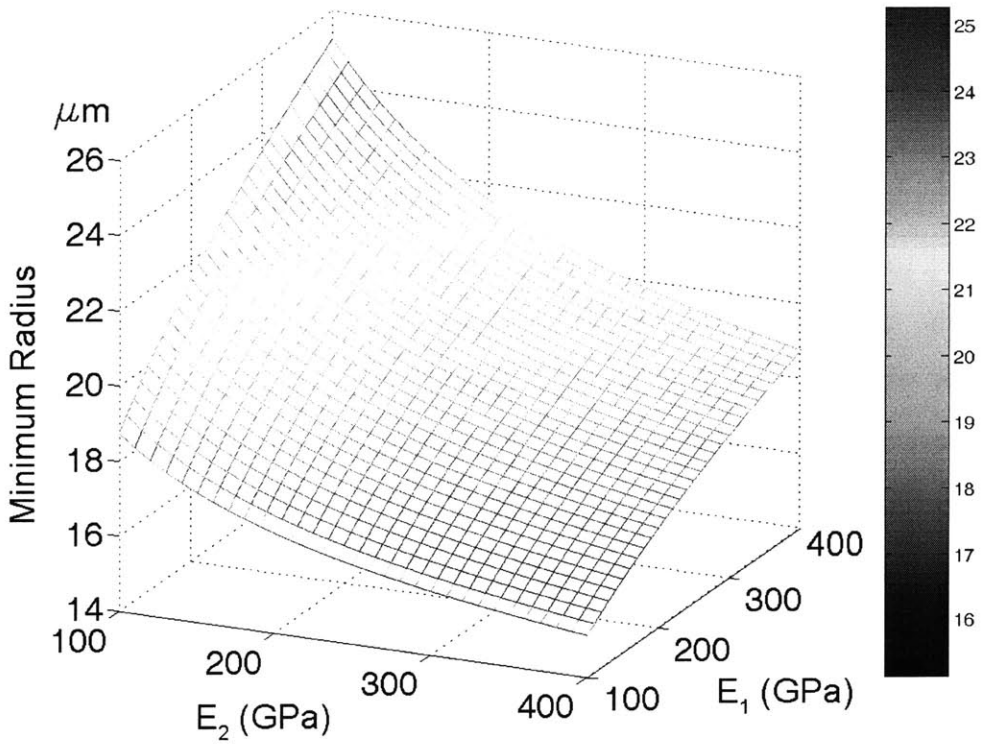

Figure 2-4: Plot of the minimum obtainable bending radius as a function of the plate modulus of the structure and stress layers for a fixed strain.

600nm. This indicates that SU-8 and perhaps other heat shrinking polymers may be even better stress layer materials than deposited metal films.

Finally, Fig. 2-5 plots the minimum obtainable radius as a function of t_1 given E_1, E_2, and C. The minimum radius scales linearly with t_1 which agrees with our intuition that the bending radius should decrease proportionally to the film thickness. The slope of the line in Fig. 2-4 depends on E_1', E_2', and C and was plotted using the aforementioned parameters.

2.4 Comparison to Other Models

Others have analyzed stress bilayer curling. Nikishkov [36], Grundmann [8] and Cybulski [37] each present a formula for the bending radius.[4] Each was derived using different mechanical principles yet surprisingly they all agree. The formulae are re-

[4]Tsui [38], Vorob'ev [5] and Vaccaro [32] present formulae that are incorrect; this has been established by analysis and confirmed via email correspondence.

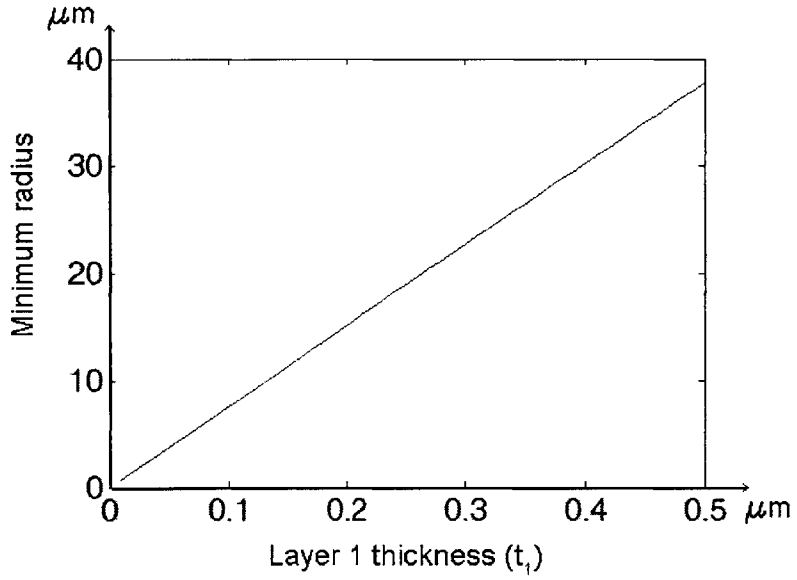

Figure 2-5: Plot of the minimum obtainable bending radius vs structural layer thickness. The slope of the line is 72.

copied with the notation used in this chapter:

$$\rho = \frac{E_1'^2 t_1^4 + E_2'^2 t_2^4 + 2E_1'E_2' t_1 t_2 \cdot (2t_1^2 + 3t_1 t_2)}{6E_1'E_2' t_1 t_2 (t_1 + t_2) \cdot (C/E_2')} \quad (2.13)$$
(Nikishkov)

$$\rho = \frac{t_1^4 + 4\frac{E_2'}{E_1'} t_1^3 t_2 + 6\frac{E_2'}{E_1'} t_1^2 t_2^2 + 4\frac{E_2'}{E_1'} t_1 t_2^3 + t_2^4 (\frac{E_2'}{E_1'})^2}{6C\frac{E_2'}{E_1'} t_1 t_2 \cdot (t_1 + t_2)} \quad (2.14)$$
(Grundmann)

$$\rho = \frac{t_1 + t_2}{6C\frac{E_2' t_2}{E_1' t_1} \cdot (\frac{t_2}{t_1} + 1)^2} \cdot [4(1 + \frac{E_2' t_2}{E_1' t_1}) \cdot (1 + \frac{E_2' t_2^3}{E_1' t_1^3}) - 3(\frac{E_2' t_2^2}{E_1' t_1^2} - 1)^2] \quad (2.15)$$
(Cybulski)

Eq. 2.13 is identical in form to Eq. 2.11 derived in Section 2.2. Eqs. 2.14 and 2.15 can also be symbolically manipulated into the exact form of Eq. 2.11; therefore, all three independent results agree.

Cybulski is the only one to analyze the formula and provide criterion for minimizing the bending radius. His film thickness optimization is recopied with the notation of this chapter:

$$t_2 = t_1 \sqrt{\frac{E_1'}{E_2'}} \quad (2.16)$$

This equation was calculated by assuming that the minimum radius is obtained when

there is zero net stress at the interface between the two layers. In most cases, the interface between the layers will actually be the surface of maximal stress (see Fig. 2-2). Eq. 2.16 is clearly incorrect when compared to minimum radius values taken from plots of the bending radius formula (for example, compare to Fig. 2-3).

2.5 Criticism of Model

The model may substantially deviate from reality if any of our approximations or assumptions were inaccurate. In this section, our model is criticized by carefully analyzing our assumptions.

Our initial conditions assumed a uniform plane stress in the upper layer. Chapter 3 presents data from the literature on evaporated chromium that indicates the stress only develops in plane. However, the mean stress in evaporated chromium has been observed to decrease from 2GPa in 25nm thick films to 1GPa in 300nm thick films. Our measurements (described in Section 3.2.2) found the mean stress in a 50nm film to be 1.7GPa and the mean stress in a 100nm film to be 1.3GPa. Therefore, there is a significant possibility that the residual stress is not uniform and is a function of the thickness t_2. This can easily be incorporated into the beam bending formula by assigning the function to $\sigma_2(y)$; however, the correct function is completely unknown.

A second major assumption was made when we applied Hooke's law to solve for the strains in the structure. This assumes that both materials behave perfectly elastically. Since the stress layer has a large initial stress that only decreases as the bilayer curls, the elastic assumption is reasonable. Plastic behavior only occurs when stress is increased beyond the material's yield point. Decreasing stress always results in elastic behavior. In the structural layer, the stresses generated must be carefully examined to analyze whether they exceed the material yield strength. In case they do, a better model for the structural layer would be elastic-perfectly-plastic. Mathematically, this would involve setting a ceiling on the stress within the structural layer and the effect would be to increase the calculated bending radius. In our experiments, we used silicon rich silicon nitride as the structural layer. From Table 2.1, silicon rich

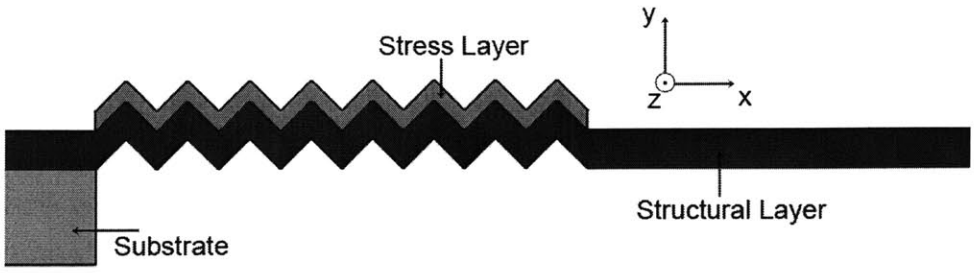

Figure 2-6: This corrugated hinge design makes two improvements over the flat layer design. First, the surface area of the stress layer is increased by a factor of 1.4 which should decrease the bending radius by a factor of 1.4. Second, the corrugations will completely prevent the hinge from curling about the x-axis.

silicon nitride has a yield strength of 9GPa which is much larger than the maximum stress caused by the bending (approximately 1-2GPa). Single crystal silicon has a yield strength of 4GPa and polysilicon has a yield strength of 3GPa, both of these materials would also be ideal elastic structural material. Silicon dioxide has a yield strength of only 70MPa and would definitely not behave elastically. In order to model it correctly the plastic deformation would have to be accounted for.

2.6 Summary and Future Work

With the practical assumptions that E_1', E_2' and C are fixed (due to material choices in experiment), we conclude that it is possible to minimize the bending radius and thus achieve the smallest possible hinge by choosing t_2 according to Eq. 2.12. If there is any freedom to choose different materials, the stress layer should have the smallest plate modulus possible to further reduce the bending radius. Finally we observe that the bending radius can be reduced by decreasing t_1. (At the same time, however, decreasing t_1 also decreases the structural strength of the hinge).

Future modeling work will examine the effect of choosing non-constant functions for $\sigma_2(y)$ and also try to model non-rectangular hinge geometries. For example, we would like to model the bending of a corrugated hinge (Fig. 2-6) and a periodically perforated hinge to see if they can better constrain the folding about a single axis and reduce the bending radius.

Chapter 3

Characterizing the Residual Stress in Evaporated Metals

In order to fully understand stress-actuated folding it is also necessary to characterize and model the residual stress in evaporated metals. This chapter discusses the cause of residual stress in evaporated metals, explains why we chose chromium for the experiments of Chapter 4, and presents stress measurement data for chromium evaporated in the MIT Nanostructures Lab (NSL).

3.1 Cause of Residual Stress

Residual stress in deposited thin film metals has been studied since the 1960s and is well understood [25]. A general trend that has been observed for nearly all metals, independent of deposition method, is that the residual stress in deposited thin films is inversely proportional to the ratio T/T_m where T is the absolute temperature of deposition and T_m is the (absolute) melting point temperature. For reference, a table of melting points for common metals is listed in Appendix A along with the ratio T/T_m at room temperature. Tungsten and chromium have the highest melting points, and have been observed to be deposited with the highest residual stresses whether deposited by electroplating, sputtering or evaporation.

The total stress in a deposited thin film consists of thermal stress and intrinsic

stress. The thermal stress is due to the difference in thermal coefficients of expansion between the substrate and thin film materials. The intrinsic stress is created by the microstructure formation of the film during deposition. An accumulation of periodic crystallographic flaws will lead to a large internal stress and for high melting point materials, this internal stress will be much larger than thermal stresses. At $T/T_m > 0.2$, the internal stress may be relaxed by diffusion, recovery or recrystallization of the microstructure [25]. Bulk diffusion prevents the accumulation of crystallographic flaws, recovery allows the crystalline dislocations to move by vacancy or interstitial transport, and recrystallization allows the strained crystal grains to reform into strain-free grains. Appendix A lists the ratio T/T_m for common metals at room temperature. Metals with high melting points include tungsten, chromium, molybdenum, nickel, iron, titanium, tantalum, platinum, rhenium and niobium. Of these, chromium and tungsten have been observed to deposit with the highest residual stress when evaporated [23, 25, 39]. In addition, they are highly etch resistant which makes them ideal choices for the release etch step in the stress-actuated folding process. We decided to investigate chromium in this thesis because it was readily available in the NSL. However, tungsten is equally promising and worth experimenting with in the future.

3.1.1 Intrinsic Stress

At low T/T_m, columnar growth has been observed in evaporated thin films [26]. Deposited metal atoms are incorporated into the coating at points close to their point of arrival, creating grains in the microstructure. TEM studies have shown that the size of these grains is proportional to the substrate temperature [24]. The grains grow vertically and remain separated by a thin boundary. The surface energy between the grain boundaries is what causes the large tensile stress, and the columnar growth ensures that the stress is constant through the thickness of the film [25]. Fig. 3-1 illustrates this concept. At lower substrate temperatures the grains will be smaller and there will be more grain boundaries; hence a larger tensile stress. The intrinsic stress is independent of the substrate material provided that the metal film adheres well to the substrate. If not, slipping at the material interface will reduce the intrinsic

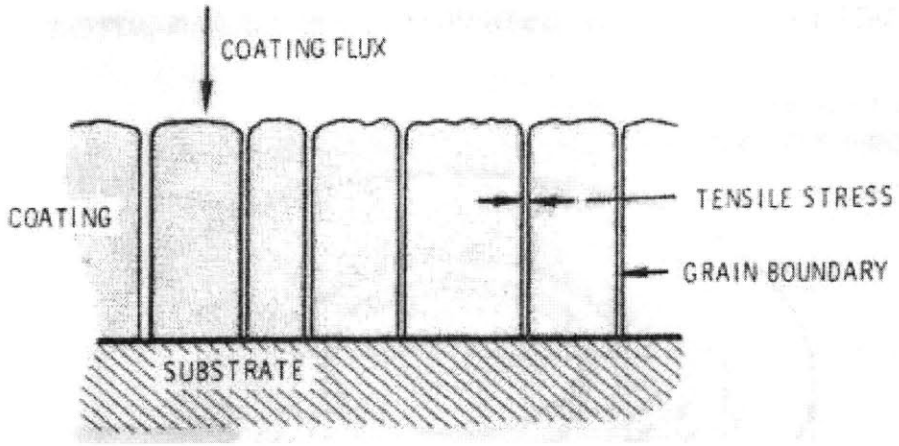

Figure 3-1: Model of intrinsic stress formation in evaporated chromium, illustrating the formation of grain boundaries and the columnar growth process. (After [25].)

stress in the metal film. For highly adhesive metals such as chromium, titanium, and tungsten, slipping is not a problem.

Although temperature is the variable that most affects the intrinsic stress in evaporated thin films, chamber pressure, chamber gas composition and rate of evaporation will also affect the intrinsic stress. Gas composition and partial pressure in the evaporation chamber have a significant effect on the microstructure formation in the film and vastly changes the intrinsic stress [24, 26]. Unfortunately, no studies have been conducted that vary gas pressure with the substrate kept at room temperature. Data taken from all the sources cited in this section indicates that the residual stress in evaporated chromium is consistently about 2GPa (tensile) when the chamber pressure is $< 10^{-4}$Pa. No studies have investigated the residual stress in evaporated chromium as a function of the deposition rate and the effect is unknown.

3.1.2 Thermal Stress

If the metal is deposited at room temperature there will be no thermal stress. However, if the temperature is changed afterwards, for example during the normal course of operation of the fabricated device, thermal stresses will arise. The strain due to thermal stress is

$$\Delta CTE \cdot \Delta T = \varepsilon_T \tag{3.1}$$

where ΔCTE is the difference in material thermal expansion coefficients, ΔT is the change in ambient temperature, and ε_T is the thermal strain. The intrinsic strain from deposition was calculated in Section 2.2 as

$$\varepsilon_I = \frac{C}{E_2'}.$$

Using CTE values taken from Table 2.1 for silicon nitride and chromium, we find that

$$\begin{aligned} \varepsilon_T &= 2.4 \cdot 10^{-5}\,^{\circ}\mathrm{C}^{-1} \cdot \pm 20^{\circ}C \simeq 0.05\% \text{ strain} \\ \varepsilon_I &= \frac{2\mathrm{GPa}}{146\mathrm{GPa}} \simeq 1.4\% \text{ strain} \end{aligned}$$

Although the thermal strain is much smaller than the intrinsic strain, this analysis shows that thermal strain resulting from atmospheric temperature variation could easily alter the bending radius by as much as 4% or more. Therefore the bending radius (which is inversely proportional to strain, Eq. 2.11) may fluctuate by 4% or more with atmospheric temperature variation. This clearly demonstrates that a latching mechanism is required to fix the membranes in place after they are folded to prevent them from changing position.

3.2 Measuring the Residual Stress in Electron-Beam Evaporated Chromium

The goal of this experiment was to measure the variation in chromium stress from separate evaporations to test its repeatability. Therefore, all other variables including chamber pressure and deposition rate were fixed.

3.2.1 Experimental Procedure

In most other experiments in the literature [24, 26], the stress of the evaporated film is measured in situ with a glass deflection beam. Lacking access to such equipment, we calculated the stress by measuring the difference in wafer curvature before and

after the chromium evaporation. The wafer surface profiles were measured using a Shack-Hartmann interferometer, and the curvature of the wafer was fitted to Zernicke polynomials. The details of this method are thoroughly discussed by Chang [40] and will not be copied here.

Six silicon wafers were evaporated with chromium at different times spread out over the course of one month. Three of the wafers were evaporated to a nominal thickness of 50nm and three were evaporated to a nominal thickness of 100nm. In between runs, the evaporator was used as usual for depositing other materials. The wafers used in this experiment were covered front and back with 200nm silicon nitride because that was the structural membrane used in the experiments of Chapter 4. Our evaporator is a Temescal BJD-1800 (made in 1980).

It was extremely important to keep the pressure and deposition rate fixed because their effects on the residual stress are not well known. The minimum pressure obtainable in our evaporator was $2.7 \cdot 10^{-5}$Pa and the rate was fixed at $5\text{Å}\cdot\text{s}^{-1}$. Unfortunately, for the first ten seconds of the evaporation, the pressure rose to 10^{-4}Pa and the rate fluctuated $\pm 20\%$ during the entire evaporation. This uncontrollable fluctuation may have contributed to variation in the stress between runs. A simple way to prevent this from occurring would be to use a shutter to block the evaporation until the pressure and rate stabilized. However, our evaporator was not compatible with a shutter.

3.2.2 Experimental Results

The results of the experiment are presented in Table 3.1. The stress is calculated using a modified Stoney's equation [40],

$$\sigma = \frac{2E_1' {t_1}^2}{3t_2 r^2} \cdot \frac{\Delta Z_{21}}{2} \tag{3.2}$$

where E_1' is the plate modulus of the silicon wafer (180 GPa), t_1 is the wafer thickness, r is the radius of the wafer, t_2 is the chromium film thickness and ΔZ_{21} is the change in coefficient of the Z_{21} term in the Zernicke polynomial. The data in Table 3.1 shows

Table 3.1: Stress measurement data. The film stress values were calculated using Eq. 3.2.

Wafer #	**Wafer radius (mm)**	**Wafer thickness (μm)**	**Film thickness (nm)**	ΔZ_{21}	**Film stress (GPa)**
1	44	390	62	16.73	1.27
3	44	390	62	18.70	1.42
5	44	390	62	19.09	1.45
2	44	390	120	28.56	1.12
4	44	390	120	24.87	0.98
6	44	390	120	30.39	1.19
7[a]	36.4	500	24	4.09	1.93

[a]This data point is from a separate experiment by Chang [40] using the same evaporator.

substantial variation in stress between evaporations. The variation may be a product of error in measuring any of the variables used to compute the stress. The wafer radius was measured to within 0.1mm; error from this variable can be neglected. The wafer thickness was measured with a caliper to within $\pm 5\mu$m; this term is squared in Eq. 3.2, so the maximum error it generates is $< 2\%$. The film thickness was measured using a Dektak profilometer with 1nm precision; this term is raised to the -1 power in Eq. 3.2, so the maximum error error it generates is $< 1\%$. The ΔZ_{21} term is fitted from the optical measurements of the wafer surface and is accurate within 1%. Since it is a linear term in Eq. 3.2 it will generate $< 1\%$ error. Therefore we conclude that at maximum, the variation in calculated stress due to measurement error is $< \pm 4\%$.[1] More likely, however, the variation due to measurement error is negligible because the wafer thicknesses and chromium film thicknesses should be very consistent (as measured in Table 3.1). The total variation in the stress data points of Table 3.1 is 6.6% for the 50nm films and 10% for the 100nm films and it is reasonable to attribute all of this variation to the evaporation process.

In our experimental procedure (Section 3.2.1) we evaporated three wafers with 50nm chromium and three wafers with 100nm chromium. The film thickness is de-

[1]Another possible variable is the initial surface profile of the wafer, since the wafers were not perfectly flat to begin with. However, Elstner [30] experimentally found that the calculated stress is independent of the initial wafer surface profile.

termined by a crystal resonator within the evaporation chamber. The reason why we obtained a 62nm film instead of a 50nm film and a 120nm film instead of a 100nm film was because this crystal was calibrated incorrectly.

3.3 Analysis of Evaporated Thin Film Residual Stress for use in Nanostructured Origami

We measured the mean stress in a 120nm chromium film to be 1.10GPa ±10% and the mean stress in a 62nm chromium film to be 1.38GPa ±6.6%. Another data point taken from [40] is listed in Table 3.1; the stress in a 24nm film is 1.93GPa. The trend is that stress increases with decreasing film thickness. This agrees with the findings of others and our measured stress values also agree with other independent studies [24, 26].

This experiment provides a good understanding of the residual stress in evaporated chromium. We have made two key findings:

1. Residual stress is almost twice as large in a 25nm film than in a 100nm film.

    - It is advantageous to use thinner bilayer structures to achieve smaller folds.

2. The variation in residual stress between evaporations may be as large as ±10%

    - It will be difficult to precisely control the residual stress and therefore the bending radius. However, the residual stress is still consistent enough to enable folding within ±10%, which makes stress-actuated folding an excellent coarse positioning technique.

We have shown that it is possible to obtain a very large tensile stress by evaporating high melting point metals. The magnitude of this stress in evaporated chromium is suitable for stress-actuated folding. However, to create folds in the opposite direction we will need a compressively stressed layer. One potential method of achieving a compressively stressed layer is to sputter deposit metal at low pressure [25]. This

phenomenon is well known and many researchers [27, 28] have observed chromium to be sputter deposited with compressive stress up to 2GPa. Therefore it should be possible to create both out-of-plane and into-the-plane folds using stressed chromium in the stress-actuated folding method.

Chapter 4

Experimental Investigation of Stress-Actuated Folding and Nanostructured Origami

The Nanostructured Origami process comprises five steps:

1. Deposit and pattern a release layer.
2. Deposit and pattern the structural layer over the release layer and substrate.
3. Create hinges on the membranes.
4. Nano-pattern the membranes with functional devices.[1]
5. Remove the release layer to actuate the hinges and fold the membranes into a 3-D structure.

This Chapter presents our experimental results on the use of chromium hinges to achieve the stress-actuated folding modeled in Chapter 2. Section 4.1 examines the fabrication methods used in these experiments and demonstrates stressed-bilayer curling. Section 4.2 demonstrates that it is possible to pattern the stressed chromium into hinges which allow controllable folding. Section 4.2.5 explains our experiments with

[1]Steps three and four may be interchanged.

a release layer. Finally, Section 4.3 shows our experimental results of the full Nanostructured Origami process and demonstrates folded, nano-patterned membranes.

In these experiments, we chose silicon rich silicon nitride as the structural layer because it can be deposited without residual stress and is commonly used for making MEMS cantilevers. We chose chromium as the stress layer because it can be evaporated with large tensile residual stress. Both materials are durable and highly etch resistant which allowed us to release the structures with a long potassium hydroxide (KOH) etch that directly undercut the silicon substrate. KOH etching of silicon is highly anisotropic and allows us to release only the area directly below the the silicon nitride membranes without using a separate release layer.

4.1 First Experiment: Demonstration of Bilayer Curling

This experiment was performed to observe the bilayer curling and verify the bending radius formula (Eq. 2.11). The results provide insight into how the curling takes place and the observed bending radii closely match those predicted by theory.

4.1.1 Fabrication Procedure

200nm silicon rich silicon nitride was deposited stress-free on both sides of a single sided polished silicon wafer by LPCVD. Shipley 1813 photoresist was spun onto the nitride and patterned into cantilever shapes (see Appendix B for the mask layout). The rectangular cantilevers were aligned to the crystalline axes of the silicon wafer in one experiment, and rotated 45° to the crystalline axes in another experiment. 100nm chromium was evaporated over the wafer and lifted off in an acetone bath. In addition to serving as the stress layer, the chromium acted as a hard mask to etch the nitride in a CF_4 plasma reactive ion etch. The wafer was put into a 20% KOH bath maintained at 70°C for four hours to undercut and release the cantilevers. It was then transferred to a de-ionized (DI) H_2O bath for 10 minutes and allowed to air

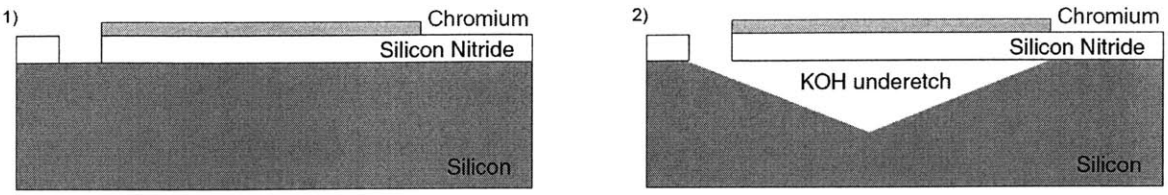

Figure 4-1: Cross-sectional view of cantilever formation, chromium deposition and KOH release etch.

dry. The fabrication procedure is illustrated in Fig. 4-1.

4.1.2 Bilayer Curling Results

The chromium and silicon nitride bilayer cantilevers curled as expected. The long KOH undercut did not visibly attack the chromium and etched the back surface of the silicon nitride by approximately $5\text{nm}\cdot\text{hr}^{-1}$. Fig. 4-2a shows a magnified view of the edge of a curled bilayer after release. The bending radius was observed to be consistent across the entire wafer. A typical front view of the curled structures is shown in Fig. 4-2b, the radius is 19μm. This agrees with the prediction by the stress-actuated folding model: substituting the appropriate material properties listed in Table 2.1 into the bending radius equation (Eq. 2.11) and assuming a 2GPa [2] stress in the chromium, we estimate the bending radius to be 21μm.

Fig. 4-3 shows an overhead view of the curling. This sample was only underetched for 90 minutes so that the KOH underetching could be observed at a mid-point in the release. The KOH undercut starts from the convex corners of the cantilever and progresses down the length of the cantilever. While the anisotropic etch is convenient because it releases only the cantilever and nothing else on the wafer, it is also undesirable because it creates stress concentration points that fracture the cantilevers. The etch planes cause diagonal curling as shown in Fig. 4-3, and cracking would occur at the center of the tip of the cantilever where the two partially undercut corners will meet.

To circumvent this problem, the experiment was repeated with the cantilevers

[2]Actually, we measured the residual stress in a 100nm Cr film to be ~1.1GPa (see Table 3.1). Section 4.2.6 explains this discrepancy.

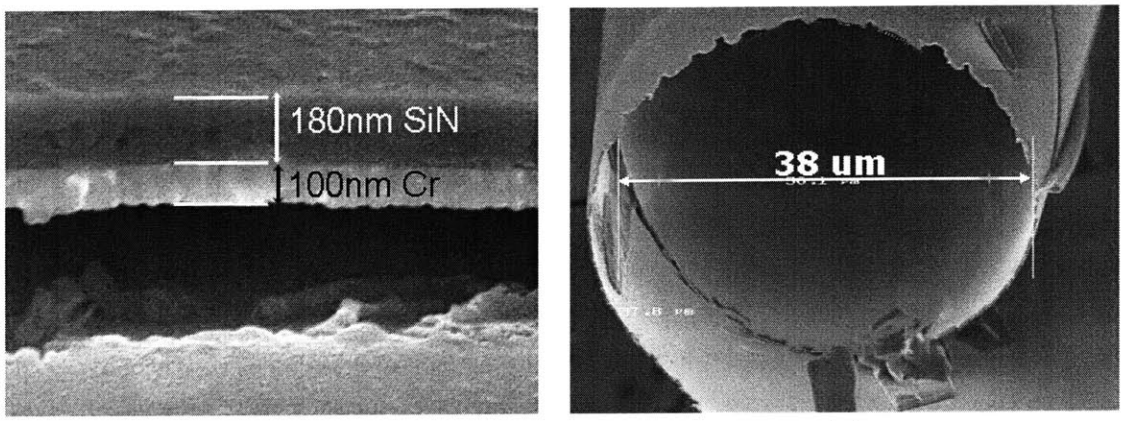

(a) (b)

Figure 4-2: (a) Scanning-electron microscope (SEM) image of the edge of a curled chromium/silicon nitride bilayer that has curled around itself more than once. The silicon nitride was 200nm thick before the etch step. (b) Front view of a curled bilayer indicating diameter. The etch trench created by the KOH undercut is visible on the left side.

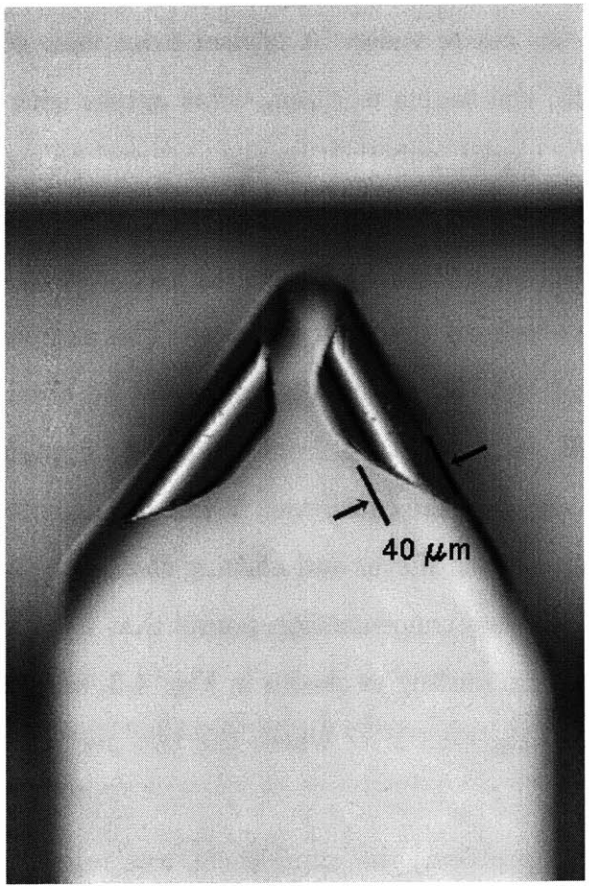

Figure 4-3: Top view of partially curled bilayer.

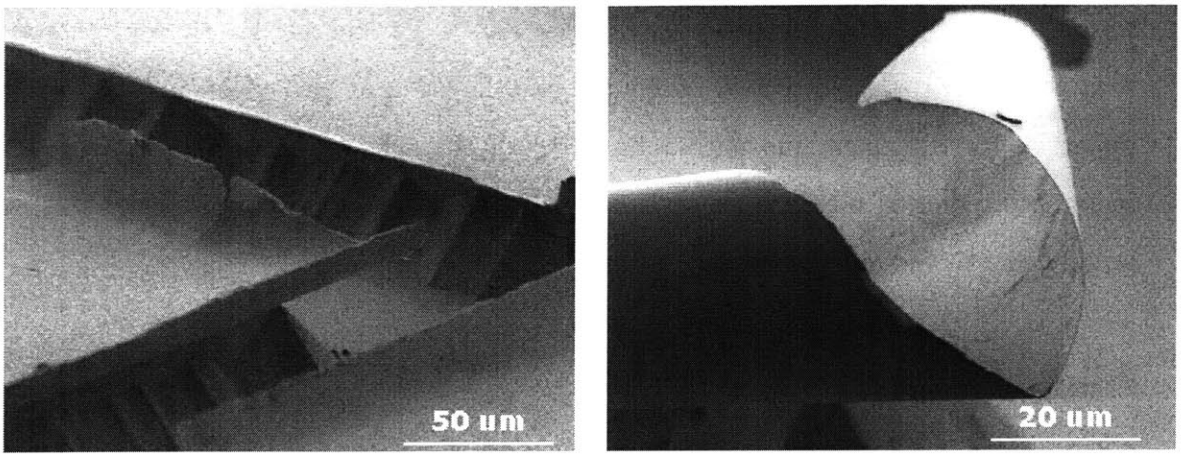

(a) (b)

Figure 4-4: The cantilevers on this sample were patterned at a 45° angle to the silicon crystalline axes. (a) Sample removed after 20 minutes. (b) Sample removed after 50 minutes.

rotated at 45° to the crystalline axes of the silicon wafer. Fig. 4-4 shows that in this case the KOH undercut the cantilevers from the edges instead of the corners, but stress concentration points still developed and produced cracking in most of the cantilevers. The bending radius observed in Figs. 4-2, 4-3 and 4-4 is consistently 19-20μm, indicating that there was little stress variation across the wafer.

4.2 Second Experiment: Patterning the Stressed Chromium to Control Folding

The purpose of this experiment was to test the hypothesis that by patterning chromium hinges of specific lengths, silicon nitride membranes could be folded to pre-determined angles. In addition to folding rectangular membranes, this experiment also investigated other shapes of membranes and hinges that could be folded. The results show that rectangular membranes can be folded controllably to pre-determined angles. We were able to fold to arbitrary angles including precisely 45°, 90° and 180°. We also observed that devices with multiple hinges folded as expected. However, the overall yield of the wafer was low, approximately 10%. The two most common failure modes

were stiction and cracking (discussed in Sections 4.2.3 and 4.2.4). However, devices that were only designed to fold in the range of 20-70° had 96% yield, indicating high potential for the technique with refinement of the release step. Most of the non-rectangular shaped membranes and hinges broke or failed to fold properly; this was largely due to the anisotropic undercut.

4.2.1 Fabrication Procedure

200nm silicon rich silicon nitride was deposited stress-free on both sides of a single sided polished silicon wafer by LPCVD. A 40nm nickel hard mask was deposited by liftoff with the template of mask 1 (see Appendix B for the mask layout and description) so that the nitride could be etched in a CF_4 plasma reactive ion etch. The nickel mask was stripped and 100nm chromium was deposited by liftoff with the template of mask 2 (see Appendix B). The wafer was put into a KOH bath maintained at 70°C for four hours to undercut the cantilevers. It was then transferred to a DI H_2O bath for 10 minutes to rinse off the KOH. After the rinse, it was transferred to an isopropanol bath for 5 minutes before being air dried. The devices were dried after being in isopropanol because it has a lower surface tension than water. The size range of devices in this experiment was so large that many were fully undercut after only one hour in the KOH etch bath. However, the extra etch time did not affect the smaller devices in any observable way.

4.2.2 Patterning Stress Results

As expected, the devices folded to an angle that was proportional to the length of the chromium hinge and the bending radius. This is described by

$$\alpha = \frac{l}{\rho} \tag{4.1}$$

where l is the length of the chromium hinge, ρ is the bending radius and α is the resulting fold angle (in radians). Figs. 4-5 and 4-6 show experimental verification of this.

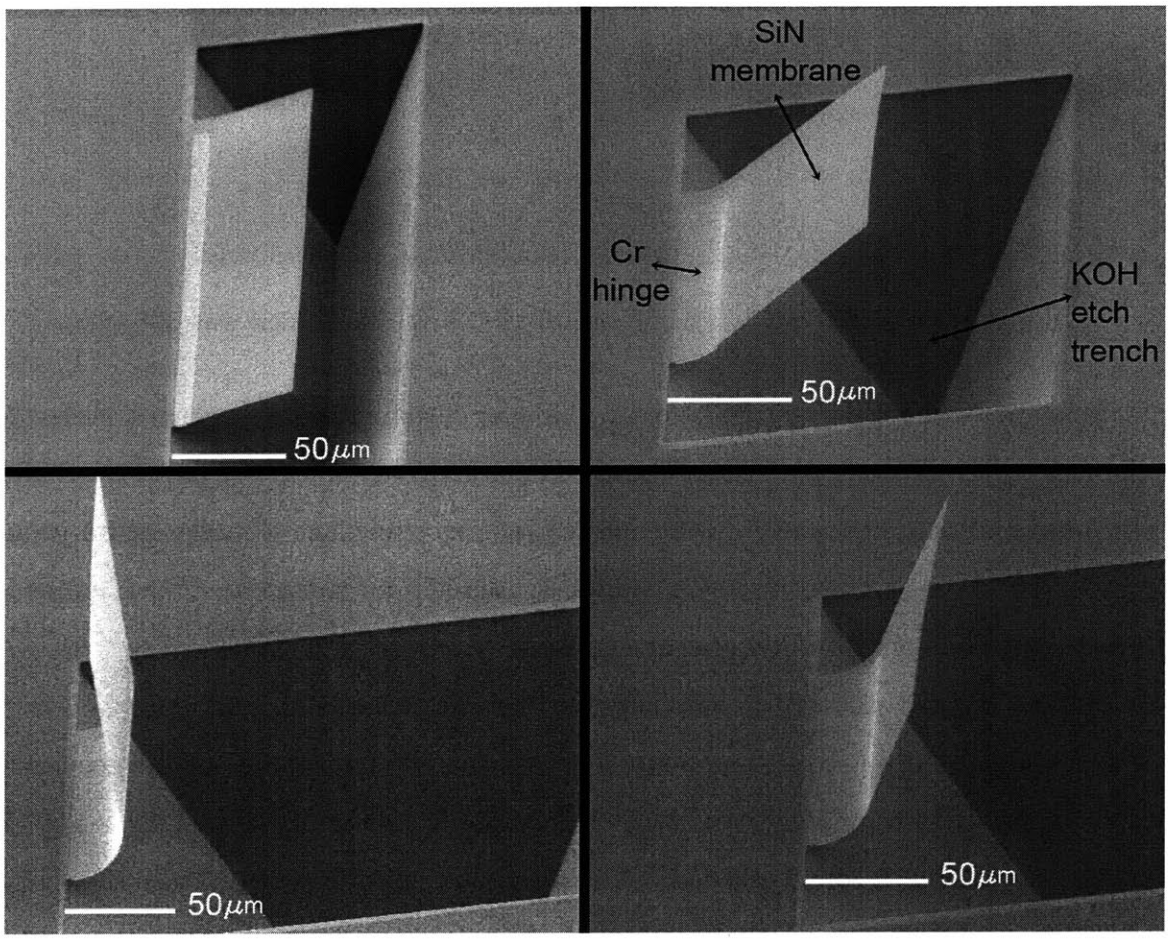

Figure 4-5: The fold angle is proportional to the length of the hinge. Data from the pictures is listed as (hinge length, fold angle). (a) 12μm, 20°. (b) 27μm, 45°. (c) 42μm, 70°. (d) 54μm, 90°.

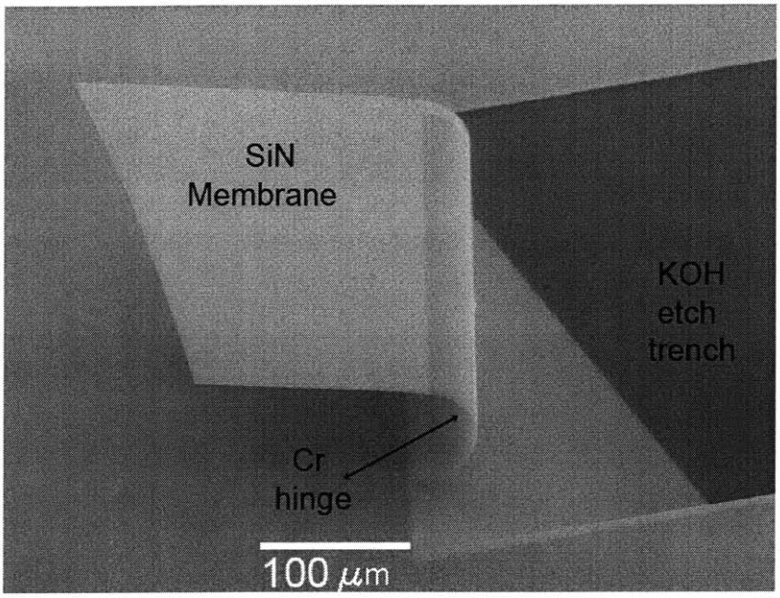

Figure 4-6: A 180° fold. The length of the chromium hinge was 100μm

It is apparent from Figs. 4-5 and 4-6 that the chromium hinges are not perfectly aligned to the silicon nitride membranes. The average alignment error on the wafer was 5μm and this was solely due to fabrication error and not a fundamental problem with the process. In future experiments, this will be corrected. The alignment accuracy of contact photolithography should be 1μm.

At this point it is worth re-emphasizing that the stress is biaxial, yet we observe folding only about one axis. The boundary condition is important, but the geometry of the hinge (width greater than twice the length) is also important. This is not an exact criterion but a rough estimate. A stressed plate bilayer will curl into the shape of lowest potential energy; therefore the curling axis will be the axis of the longer dimension. Most of the hinges in this experiment had width equal to four times the length. Fig. 4-7 shows that if the length is greater than the width, the hinges tend to twist sideways to achieve their minimum energy state.

Multiple hinges can be placed on a single membrane and the total fold angle is the sum of the individual folds. This is shown in Fig. 4-8.

Several other devices with multiple hinges were folded, including some that were almost 1mm long (Fig. 4-9). The 200nm thick silicon nitride is remarkably stiff and straight along each segment and makes an ideal structural material.

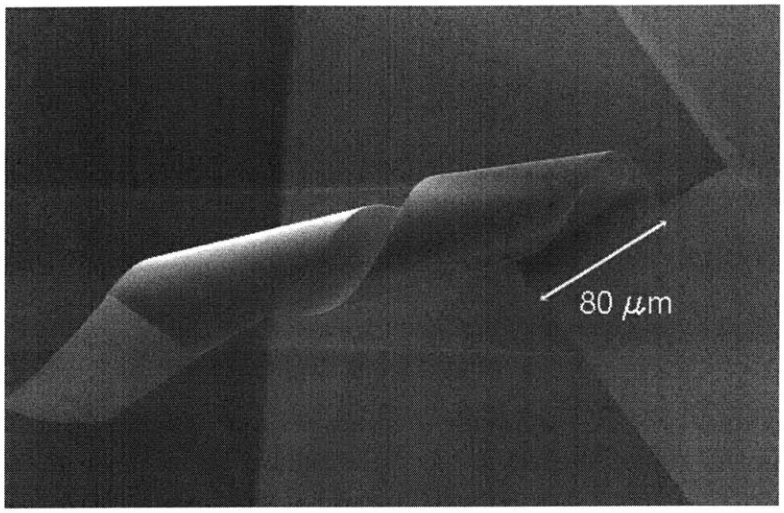

Figure 4-7: The length of this hinge is four times the width, making it unstable.

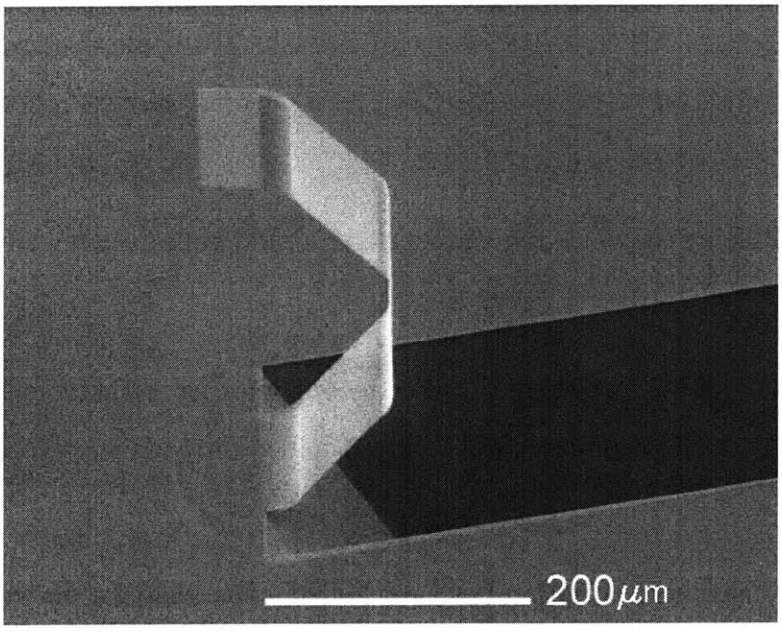

Figure 4-8: Each of the four hinges is 27μm long and has folded to 45°. The total fold angle is 180°.

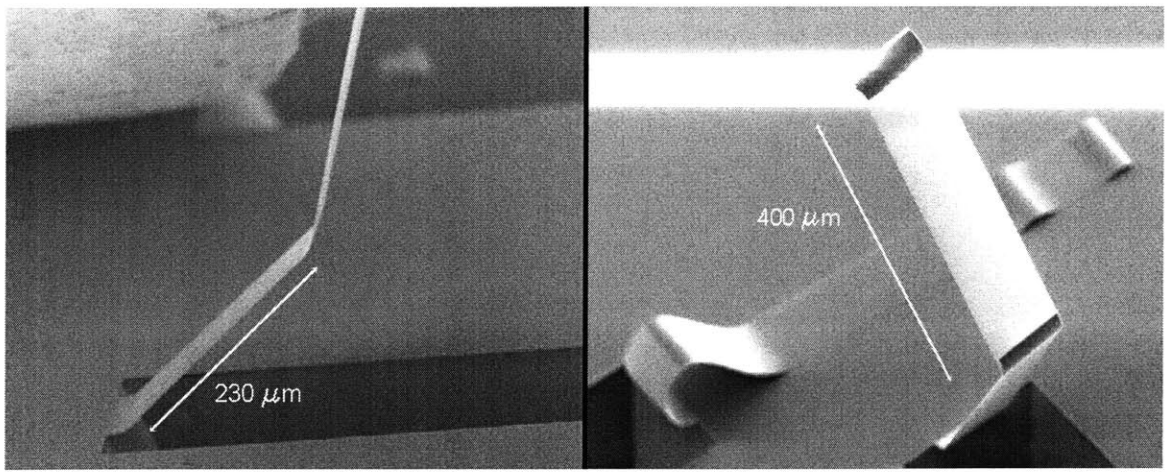

Figure 4-9: 200nm thick silicon nitride membranes were straight and stiff when folded. In the right figure, one of the devices is pulled down by stiction forces.

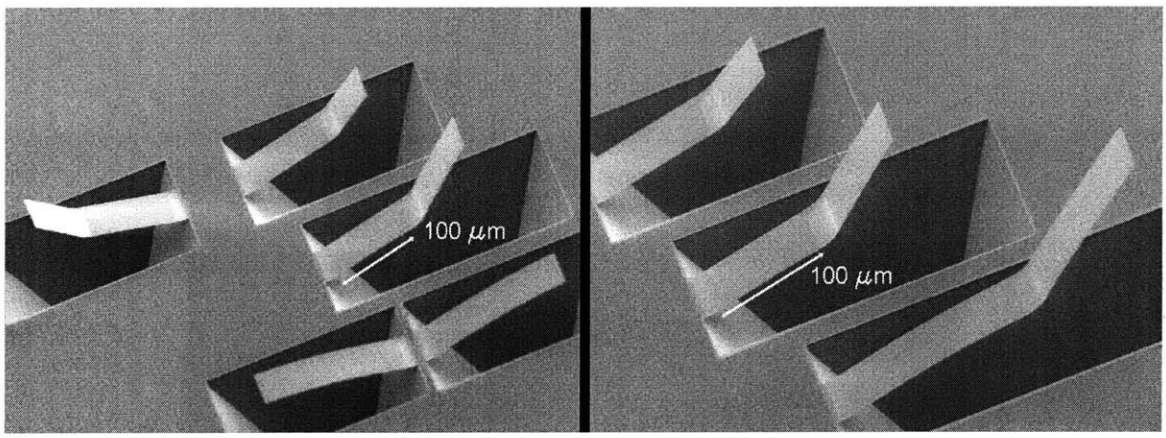

Figure 4-10: Placing the devices in close proximity did not adversely affect the process.

Devices could also be placed adjacent to one another without causing any problems. Fig. 4-10 shows two sets of devices that folded properly next to their neighbors.

We also constructed corner cubes that folded. The yield for these structures was extremely low (approximately 1%) because the anisotropic undercut did not match the cube layout well. However, Fig. 4-11 shows that it is possible to fold corner cubes and that there is nothing structurally wrong with the design; the problem is with the KOH undercut process. Improved release processes are discussed in Section 4.4.1.

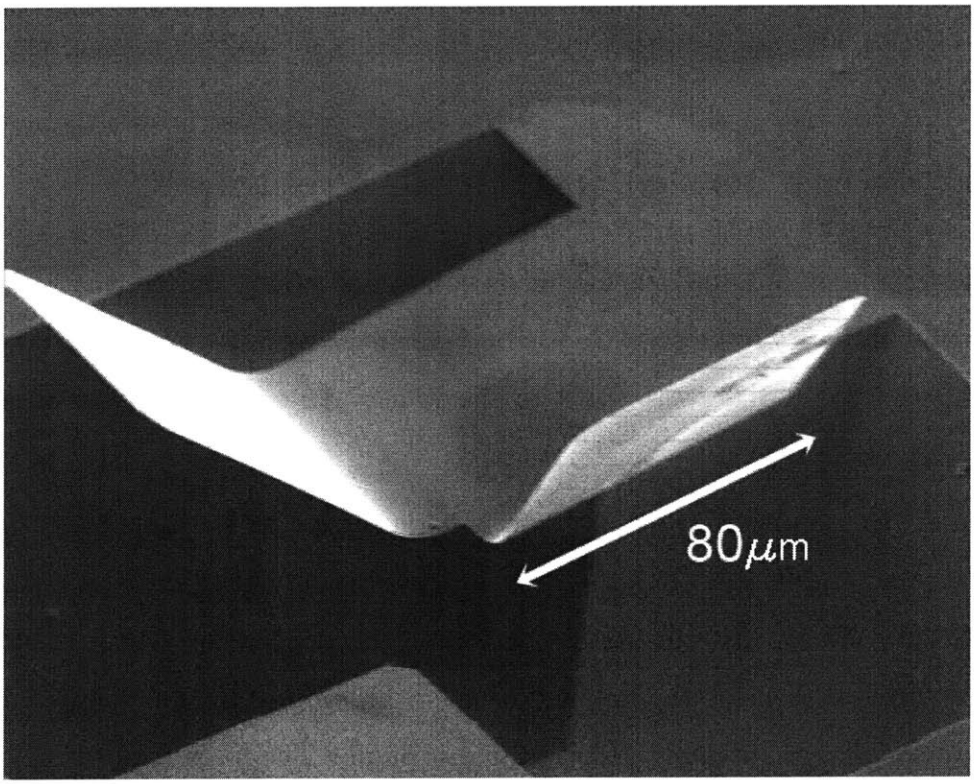

Figure 4-11: Picture taken at 45° to the substrate plane. The entire structure is underetched including the base of the corner cube. The sidewalls are folded to 60°.

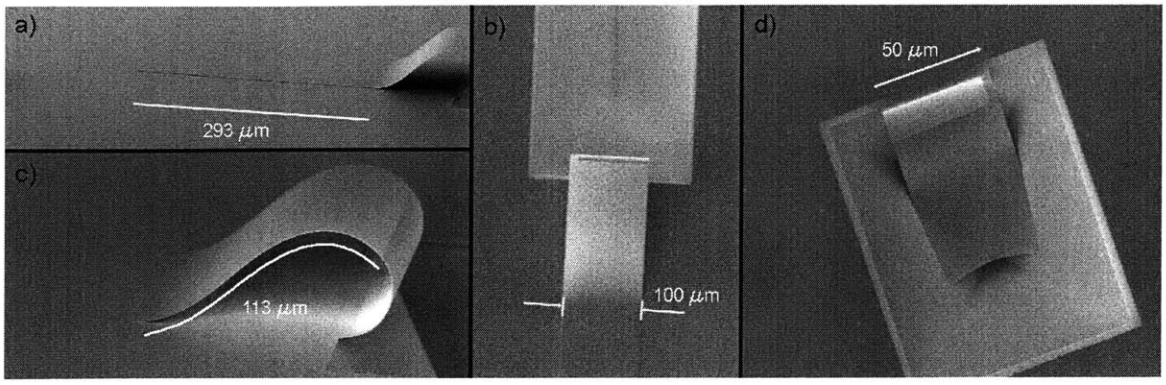

Figure 4-12: Two modes of stiction failure. (a-c) Three views of the same cantilever folded beyond 90° and stuck to wafer. (d) Cantilever folded to less than 90° stuck in trench.

4.2.3 Surface Tension and Stiction Problems

The most common failure mode for the devices was stiction. Devices that were folded to less than 60° were often stuck to the bottom of the release trench and devices that were folded beyond 120° were stuck to the wafer. An example of each is shown in Fig. 4-12.

The device pictured in Fig. 4-12a-c is folded to make an angle of 36° with the substrate and the length of the portion not in stiction is 113μm (data taken from Fig. 4-12c). We can use this data to estimate the stiction force by calculating the force required to displace the free end of a $l = 113\mu$m beam. The displacement Δd of the beam is approximately $113 \cdot \sin(36°) = 66\mu$m. The force required to deflect a cantilever beam is

$$F = \frac{E' w t^3 \Delta d}{4 \cdot l^3}. \tag{4.2}$$

This equation is valid for small deflections (~10% of the beam length). In our case the deflection is large but we will use the equation anyway just to obtain an order of magnitude estimate. The width (w) is 100μm in Fig. 4-12b and the thickness (t) is 200nm. The plate modulus of silicon nitride is approximately 326GPa. Thus, Eq. 4.2 estimates the stiction force to be 3μN. This gives an order of magnitude estimate of the stiction force to be micro-Newtons. If we estimate from Fig. 4-12c that the beam is pulling up on an effective contact area of 10x100μm then the stiction force

per unit area is approximately $10^3 \mathrm{N\,m^{-2}}$.

Stiction is a large force and has been a major challenge in MEMS research. It is a result of weak forces that become significant when two surfaces get very close (their surface separation is defined as their average rms surface roughness). The two forces responsible for stiction are capillary and van der Waals forces. Capillary condensation of water vapor occurs when two surfaces are closer together than a characteristic condensation distance. This distance is given by

$$d_{cap} = \frac{2\gamma \cdot \nu \cos(\theta)}{R \cdot T \log(RH)} \tag{4.3}$$

where ν is the liquid molar volume, RH is the relative humidity, R is the gas constant, T is the absolute temperature, θ is the contact angle of the two surfaces and γ is the surface tension of the liquid [41]. The total surface interaction energy is a function of d_{cap}. This energy can be minimized by lowering the relative humidity or by using a liquid with a lower surface tension. Reducing the relative humidity from 80% to 40% reduces the total capillary surface interaction energy by two orders of magnitude [41].

Van der Waals forces are a result of temporary dipole formations between the molecules of two surfaces. The interaction is weakly electrostatic and therefore decays exponentially with the separation distance of the two surfaces. If the rms roughness of the two surfaces is greater than 5nm, the surface interaction energy due to van der Waals forces will be insignificant. The silicon nitride membranes used in this experiment have a surface roughness of approximately 1-2nm. According to [41], this corresponds to a surface interaction energy of 1-10mJ $\mathrm{m^{-2}}$. At high RH capillary forces dominate and at low RH van der Waals forces dominate. In the NSL, the RH is 60% and the approximate surface adhesion energy between the folded membranes and the substrate is 50mJ $\mathrm{m^{-2}}$, mostly due to capillary forces [41]. When the samples are placed in a zero-humidity enviroment (for example, the strong vacuum of the SEM) the membranes remain stuck which indicates that the van der Waals forces are strong enough to maintain stiction.

To put a perspective on the magnitude of the stiction surface energy, Fig. 4-13

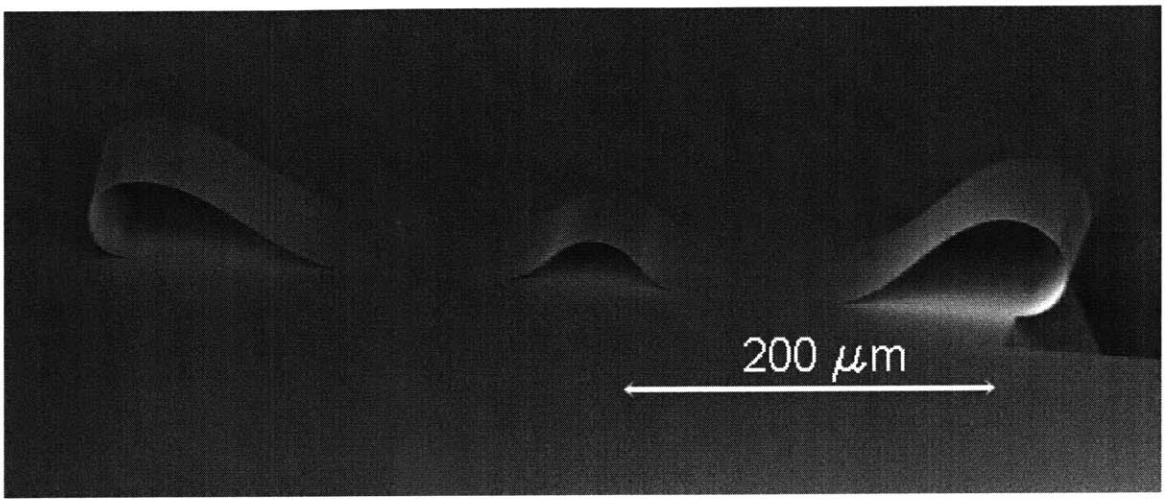

Figure 4-13: The entire center portion of the membrane is in stiction except the hinge which is not at all deformed by stiction.

shows that they are much less than the surface energy in a bent bilayer hinge. The total energy per unit surface area in a plate of thickness t, plate modulus E', and strain ε is

$$\frac{W}{A} = \frac{1}{2}\int_0^t E' \cdot \varepsilon^2 \mathrm{d}t\,. \tag{4.4}$$

For a 100nm chromium plate with an initial strain of 1%, the energy per unit area is approximately 700mJ m^{-2}. In order to keep the hinge flat and stuck to the substrate, stiction surface interaction energy would have to exceed this number. However, even at 60% humidity stiction is more than an order of magnitude weaker (see above estimate). This means that we should be able to scale down the size of the hinges by almost an order of magnitude (and therefore the radius as well) without worrying about stiction forces destroying the hinges.

We observed empirically that devices which were in stiction immediately after drying could not be unstuck by mechanical probing, air currents or electrostatic charging. Devices that were freestanding after drying could be pushed into contact with the substrate and adhere due to stiction. However, these devices could be easily unstuck by mechanical probing, air currents and electrostatic charging. This result suggests that the major problem is in the drying step. The surface tension of the drying liquid pulls a large portion of the membrane surface into close contact with the substrate, whereas

when the membranes are mechanically pressed into the substrate only a small area of the membrane comes into close contact. For example, the energy required to separate a 100x100μm membrane that is entirely stuck is 100 times greater than the energy required to separate a membrane in which only a 10x10μm area is stuck. To minimize the surface tension while the devices were drying, they were rinsed in isopropanol immediately after the water rinse. The surface tension of isopropanol is 22mJ m^{-2} compared to the surface tension of water which is 77mJ m^{-2}. A common solution to avoid surface tension entirely is to dry the sample in a supercritical or triple point dryer. When we experimented with a supercritical dryer we observed that few devices were pulled into stiction by surface tension. However, the supercritical dryer (which was not in a clean room environment) left a film-like residue behind over the entire sample that could not be removed, rendering the tool unsuitable for our experiments.

4.2.4 Cracking Problems Due to Anisotropic Etching

The second most common failure mode for the devices was cracking. We observed a similar pattern of cracking in almost all of the failed devices. Fig. 4-14 shows triangular cracking and angled cracking along 45° lines. This is a direct consequence of the KOH undercut process. Fig. 4-3 shows how the etch progresses from the corners forming a triangle. As the KOH undercuts the chromium hinges, the sides are released and bend upwards while a triangular portion at the center remains attached to the substrate. Cracking then occurs along this still connected edge. This effect was more pronounced in the wider devices which consequently had more edge area that could fold up before the center was released.

4.2.5 Comments on the Release Process

Ideally, the release should progress uniformly down the length of the cantilever. In reality there is no release material and etchant combination that will produce this effect. Even if the underetch is completely isotropic, stress concentrations will occur because the undercut progresses from all three sides (similar to the undercut of Fig.

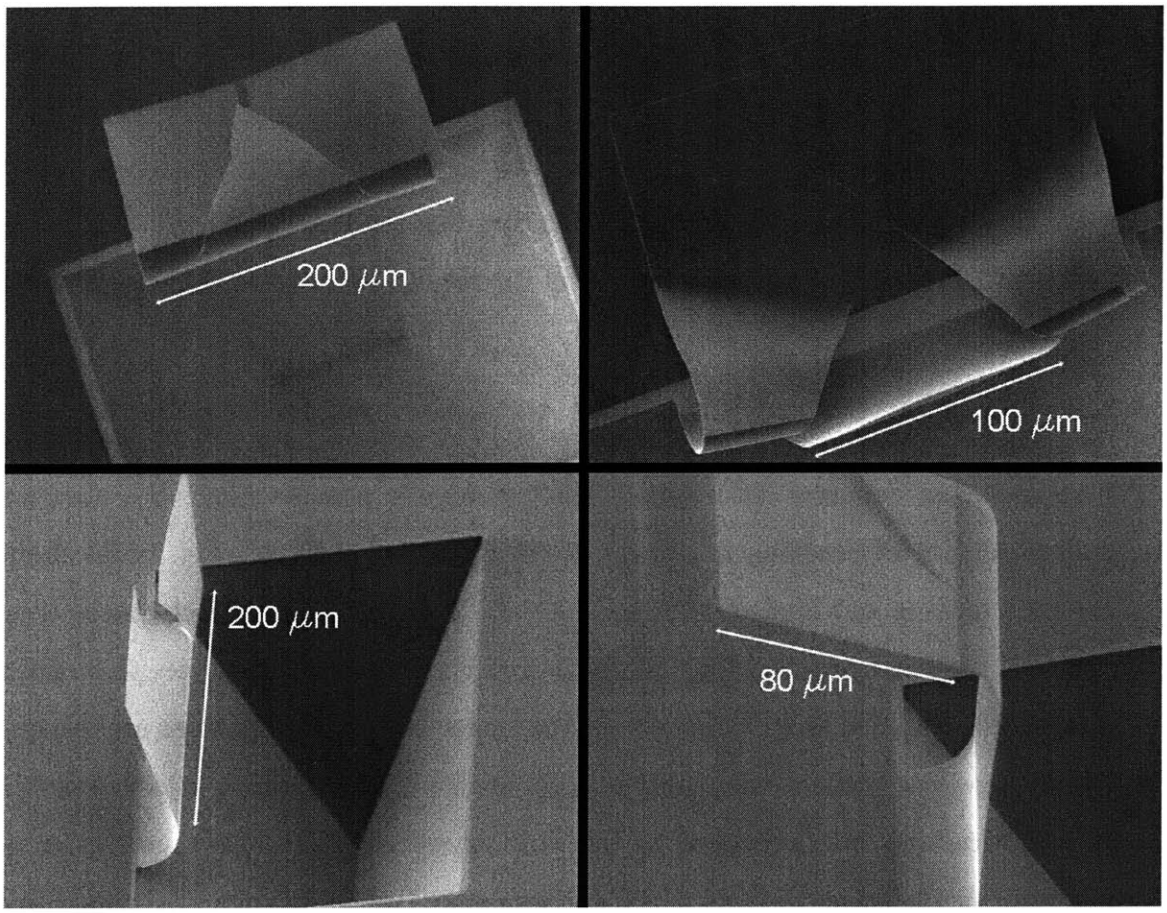

Figure 4-14: Several examples of the triangular cracking.

4-4). The hinge at the base of the cantilever would release from the sides, fold partially and crack. One way to circumvent this problem is to pattern etch holes into the structural layer (in addition, etched holes may serve as periodic dielectric discontinuities for the fabrication of a photonic crystal). Alternatively, one can pattern photoresist over the entire substrate with the mask used to define the membranes. The thick photoresist layer will prevent the device from curling during the release step. After the release step is finished, the substrate can be heated to melt away the photoresist and allow the hinge to relax its stress uniformly. This technique has been recently demonstrated by Chua [11].

4.2.6 Residual Stress Variation

All of the devices in this experiment had a 34μm bending radius (calculated from Fig. 4-5). This is much larger than the 19μm bending radius observed in the first experiment (see Fig. 4-2) and predicted by the model. The only processing difference between this experiment and the first experiment was that the chromium layer was never used as a hard mask for a reactive ion etch. According to the stress measurements of Section 3.2.2, the intrinsic stress in a 100nm chromium film deposited with the NSL evaporator is 1.1GPa (not 2GPa that was assumed in the model of Chapter 2). Recomputing the bending radius (from Eq. 2.11) with an initial stress of C =1.1GPa predicts a 35μm radius and the results of this experiment are more consistent with the model. Thus it is highly likely that the reactive ion etch step in the first experiment (Section 4.1) altered the microstructure of the chromium and increased the intrinsic stress from 1.3GPa to 2GPa. This would explain the difference in bending radii between both experiments. At the time of writing, this hypothesis is still being tested and cannot be confirmed.

4.2.7 Analysis of Stress-Actuated Folding

This experiment clearly demonstrated that the stress-actuated folding concept works and has significant potential as a 3-D micro-manufacturing tool. Its demonstrated

strengths are that it is self-actuating upon release, the fold angle is controllable via lithography, and structurally stiff membranes can be folded in multiple places to form 3-D shapes.

Its main weakness is that it is based upon material properties and residual stresses that are impossible to perfectly control. The stress layer also has biaxial stress when uniaxial folding is desired, and the bending radius may be too large ($\sim$ 50-100 times the membrane thickness) to efficiently create layered devices.

Many improvements to the process have already been discussed, but the one problem that does not have any promising engineering solutions is how to precisely control the radius of curvature. If the film thicknesses or residual stresses vary by only 5% (a realistic margin of error), the bending radius will vary by the same and could be 9° off on a 180° fold. For designing complex 3-D shapes, this is unacceptable. Instead of trying to perfectly control the fabrication process, attention should be focused on developing adaptive controls to compensate for the fabrication error, i.e. fine alignment and latching techniques. The stress-actuated folding is excellent for approximate folding but needs a complementary system to achieve fine positioning. For this purpose we have proposed using nano-magnets. The magnets can be patterned onto the membranes lithographically and magnetized prior to folding. When the membrane folds over the magnetization direction is reversed and the magnets on the membrane and substrate attract and naturally align. With additional techniques such as this one, stress-actuated folding becomes a functional and practical 3-D micro-manufacturing tool.

4.3 Experiment Three: Folding Nano-Patterned Membranes

Thus far, the thesis has focused on 3-D micro-manufacturing and presented stress-actuated folding as a viable method. In this experiment, we prove that the silicon nitride membranes can be arbitrarily nano-patterned prior to folding. The results

demonstrate the full concept of Nanostructured Origami and show that 3-D nano-manufacturing is possible with stress-actuated folding. 340nm period gratings were written with scanning-electron-beam lithography (SEBL) and etched 80nm into the silicon nitride membranes. We etched into the nitride instead of depositing material onto it to avoid residual stress and KOH etch selectivity complications. The membranes folded as expected and the nano-patterns were preserved.

4.3.1 Fabrication Procedure

200nm silicon rich silicon nitride was deposited stress-free on both sides of a single sided polished silicon wafer by LPCVD. A 40nm nickel hard mask was deposited by liftoff with the template of mask 1 (see Appendix B) so that the nitride could be etched in a CF_4 plasma reactive ion etch. After the nitride etch, photoresist was pipetted onto devices at the corners of the wafers and over the alignment marks. The photoresist was baked and the nickel mask was stripped. The purpose of this step was to leave behind patterned metal to serve as alignment marks for the subsequent SEBL step. It is important to have metal alignment marks because it is not possible to observe patterns in 200nm thick silicon nitride with an electron microscope from an overhead view. A trilayer stack of 160nm XHRIC-16 anti-reflective coating (ARC), 20nm evaporated silicon dioxide and 100nm PMMA was spun onto the wafer. 100nm PMMA was an unsuitable etch mask for a CF_4 plasma etch into the silicon nitride because its etch rate is faster than silicon nitride. The trilayer stack was formed to transfer the pattern from the PMMA into the silicon nitride. More details on the trilayer stack are found in [42]. Grating lines were written with the SEBL using a dose of 1nC cm^{-1} and a step size of 2nm. The PMMA was developed in a 3:1 solution of isopropanol:methyl-isobutyl-ketone for 60s and the pattern was transferred into the silicon nitride by reactive ion etching [42]. The ARC was stripped with an O_2 plasma etch and the wafer was piranha / RCA cleaned to complete the nano-patterning portion of the experiment.[3] 100nm chromium was then deposited by liftoff with the

[3]We found that if the wafer was not piranha / RCA cleaned at this point, the chromium hinges would lift off from the wafer during the KOH etch step. This indicated that there was residual ARC

template of mask 2 (see Appendix B). The wafer was put into a KOH bath maintained at 70°C for four hours to undercut the cantilevers. It was then transferred to a DI H_2O bath for 10 minutes to rinse off the KOH. After the rinse it was transferred to an isopropanol bath for 5 minutes to rinse away the water, and then air dried.

4.3.2 Folding Nano-Patterned Membranes Results

The results demonstrate that it is possible to nano-pattern the planar membrane prior to folding and then fold it into a 3-D shape with no unusual difficulty. Figs. 4-15 and 4-16 highlight the major achievement of this thesis which is to controllably fold a nano-patterned membrane. The 30x30μm square patches on the folded membranes are the gratings, which can be seen when magnified. The period of the gratings is 340nm and they are etched 80nm into the silicon nitride. The duty cycle of the grating is reversed between Figs. 4-15 and 4-16. This is because the substrate was not leveled flat during the SEBL step and the electron beam was out of focus (fabrication error).

Most of the devices from this experiment were in stiction after the release step. This was due to photolithography misalignment of the chromium hinges (fabrication error). In many cases, the hinges were several microns away from the base of the cantilever which allowed surface tension forces to pull the base of the cantilever into the trench and cause stiction, as shown in Fig. 4-17.

Finally, Fig. 4-18 shows a folded device with three hinges and two nano-patterned areas. The worm-like shape of this device is caused by the bent hinges and by stiction forces. Two areas on the membrane and one on the substrate have been nano-patterned. Although this device did not fold properly, it is shows the concept of how multiple folded nano-patterned membranes may be layered or interact in 3-D.

---

left on the wafer even after the O_2 plasma strip. SEM images were taken of the wafer after the ARC plasma strip that revealed a thin layer of particles on the wafer, presumably left behind from the ARC. The particles were gone after the piranha / RCA clean.

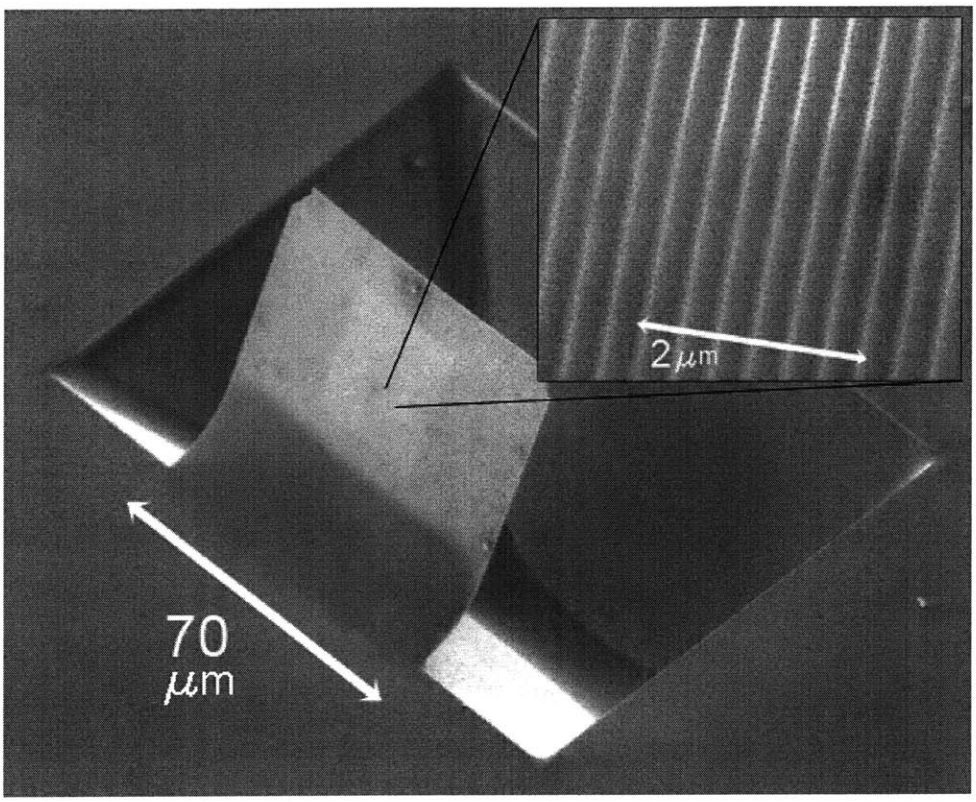

Figure 4-15: Membrane folded to 45° with a 340nm period grating at the center.

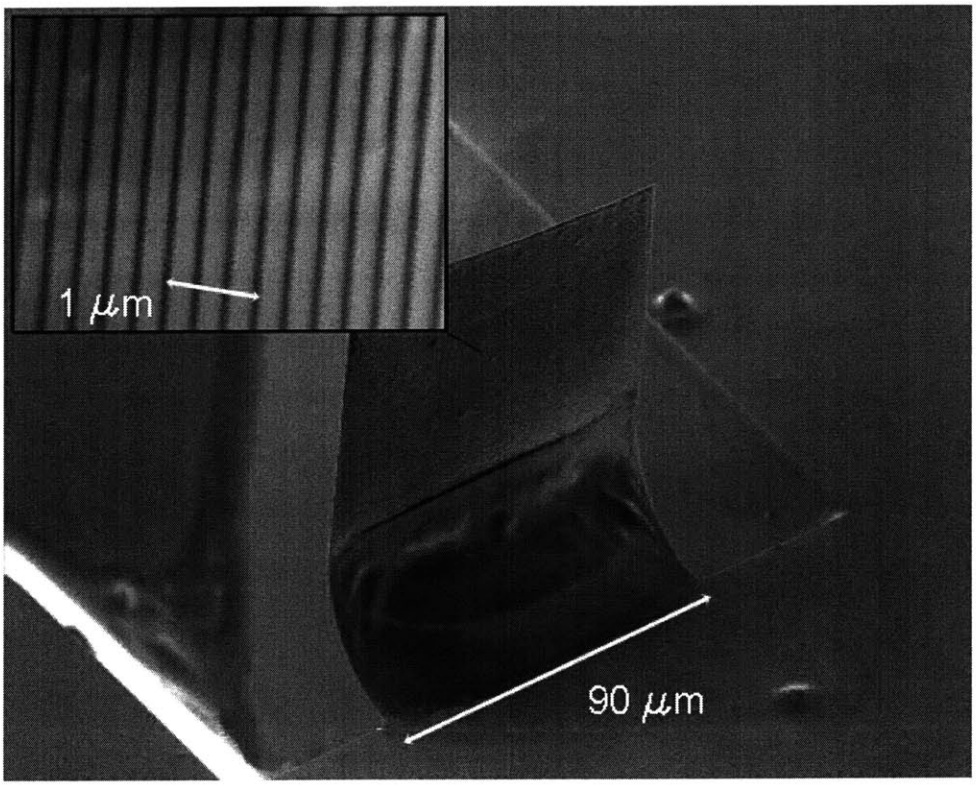

Figure 4-16: Membrane folded to 110° with a 340nm period grating at the center.

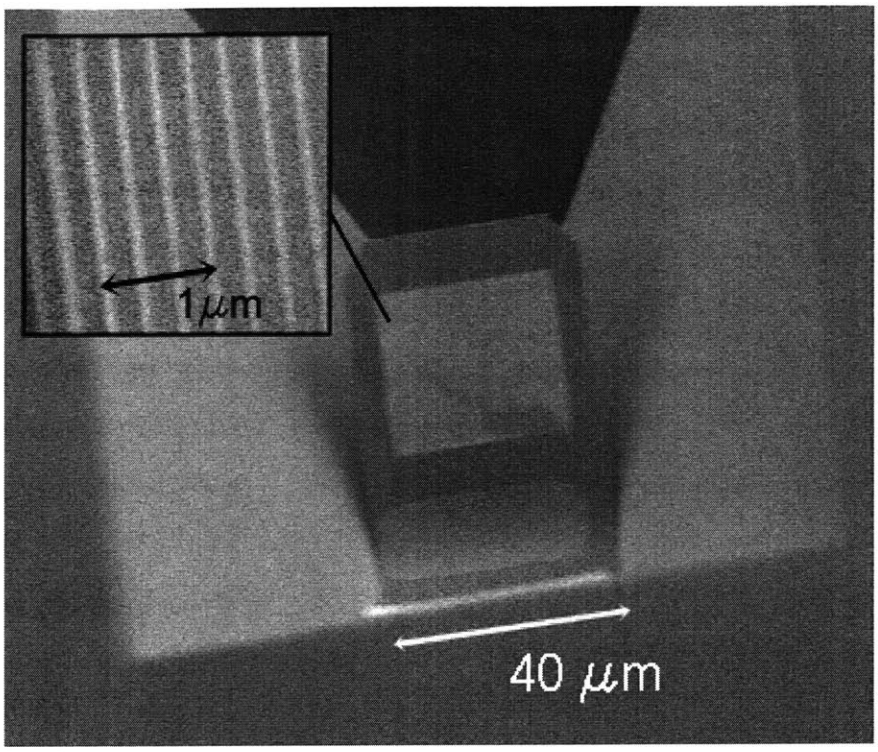

Figure 4-17: Nano-patterned membrane in stiction due to misalignment of the chromium hinge.

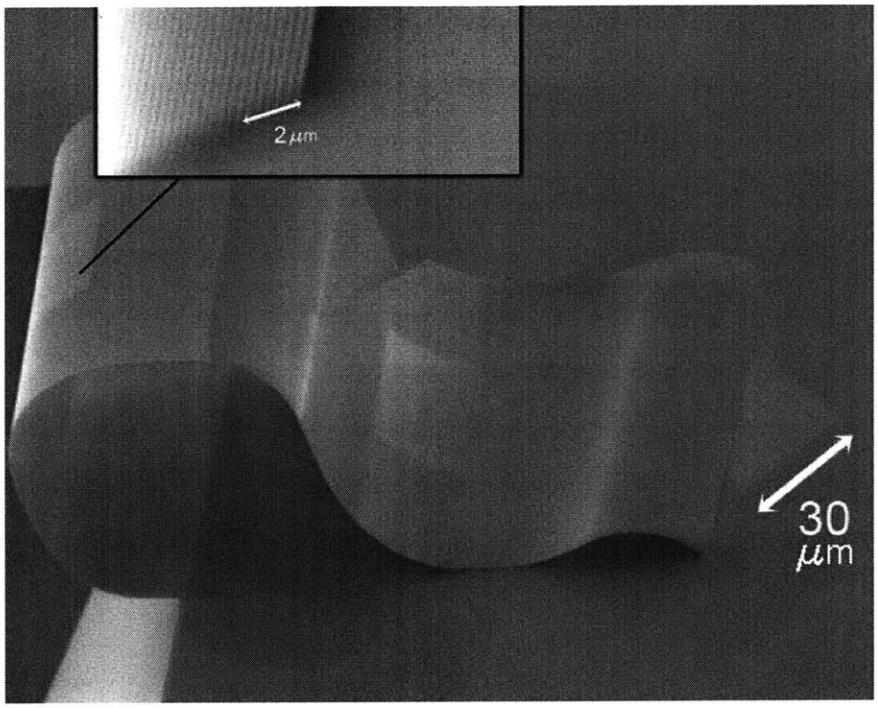

Figure 4-18: A device with multiple hinges and nano-patterns shows the concept of layered and 3-D nano-interconnectivity.

4.3.3 Analysis of Experiment

The results of Section 4.3.2 demonstrate that we were successful in folding nano-patterned membranes using stress-actuated folding. The membranes were patterned using scanning-electron-beam lithography which is capable of writing arbitrary nano-patterns. Any other nanolithography technique such as imprint lithography, interference lithography, dip-pen lithography, maskless lithography, etc. could also be used to write the nano-patterns.

It should be noted that the yield of this wafer was extremely low due to several fabrication errors. As mentioned in Section 4.3.1 the ARC caused the chromium to liftoff when the ARC was not fully stripped away. Fixing this problem without starting over affected the aligned photolithography step of the chromium hinges (the alignment marks were lost) and led to the misalignment observed in Fig. 4-17. However, in subsequent experiments these errors will be corrected and the yield should be no different than that of Experiment 4.2. The process described in Section 4.3.1 is error-free.

The next challenge that needs to be addressed is folding membranes with deposited material (instead of etched patterns). Additional stresses in the deposited material and etch selectivity with the release step will be investigated. Future experiments will also attempt to fold a purposefully designed 3-D diffractive or photonic structure to prove the usefulness of the Nanostructured Origami technique.

4.4 Experiment Four: Controlling Folding with a Release Layer

In order to avoid problems due to the anisotropic release and to avoid etching a deep trench into the wafer, this experiment investigated using a thin oxide release layer. The process flow is laid out schematically in Fig. 4-19. The fabrication procedure was identical to that of Experiment 4.2 except that prior to the silicon nitride deposition (the first step), a 100nm thermal oxide layer was grown on the wafer and patterned

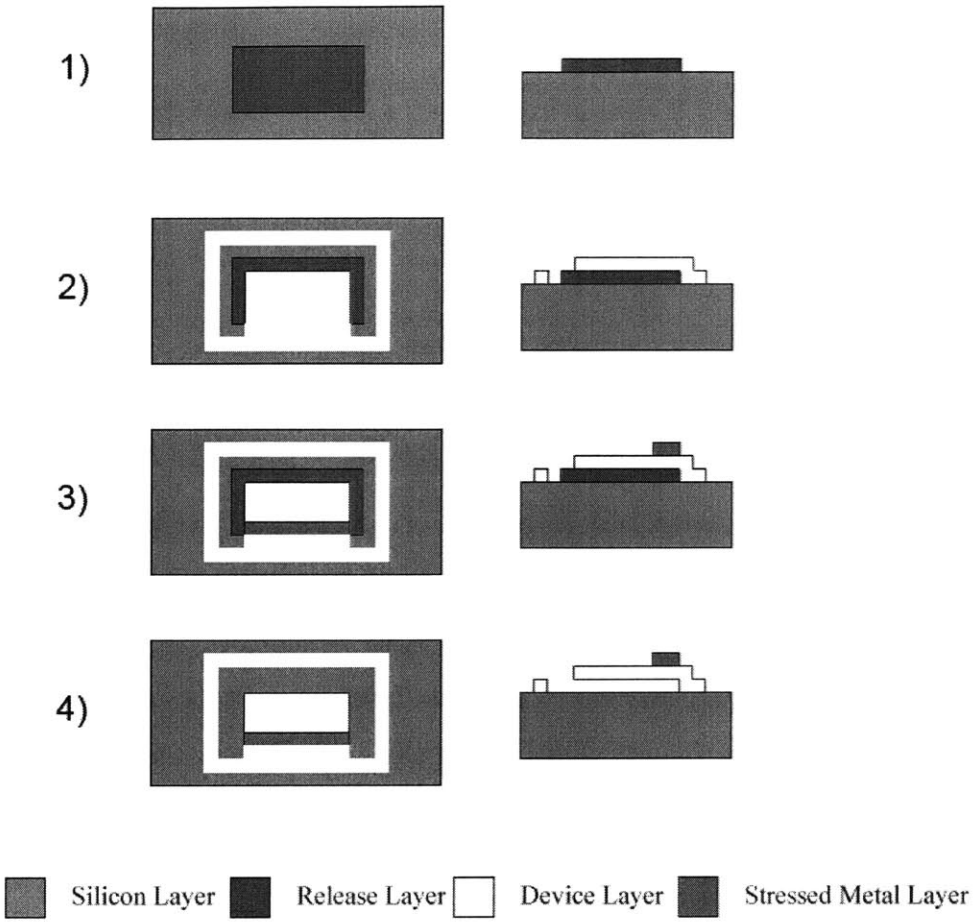

Figure 4-19: Overhead and cross-sectional view of the process flow using a release layer.

with the release mask (see Appendix B). The silicon nitride was then deposited over the 100nm thermal oxide and substrate, and the process continued as before. Also, instead of a KOH etch bath, a hydrofluoric acid (HF) etch was used. The etch rate of silicon dioxide in 49% HF is several microns per minute; it is a very aggressive etch. However, we found that the etch rate of silicon nitride in HF was not zero but approximately 10nm/min. By the time the release layer was underetched, the devices had disappeared. The oxide release layer was unsuccessful in this experiment.

4.4.1 Dry Release Processes

A dangerous and uncommon oxide etch is done by using HF vapor instead of liquid HF. The advantages of this are that it would be a dry release process (thus avoiding

stiction) and that HF vapor may not etch silicon nitride or other materials such as polysilicon and metals. A dry release process is ideal because it avoids stiction, liquid contamination and drying residues. Other dry release options include XeF_2 gas with a polysilicon release layer and Cl_2 gas with an Al release layer. These will all be investigated in future experiments.

Chapter 5

Conclusions and Future Work

The most important results of this thesis are summarized here and future work is suggested. The major contributions of this thesis are the development and analysis of the stress-actuated folding model in Chapter 2, the residual stress measurements and analysis of Chapter 3, and the experimental demonstration of the Nanostructured Origami process in Chapter 4.

5.1 Stress-Actuated Folding Model

Chapter 2 presents an analytical model of stress-actuated folding. The model provides an understanding of the mechanical principles involved and allows us to predict the behavior of a stressed bilayer. Using Eqs. 2.11 and 4.1 it is possible to calculate the length of the chromium hinge necessary to fold the membrane to a desired angle. This is extremely useful for designing the photolithography mask layouts used in experiment.

The analysis of Section 2.3 presents criteria for minimizing the bending radius (Eq. 2.12 and Fig. 2-4). Applying these criteria allows us to determine the optimum chromium film thickness to achieve the smallest possible hinge in experiment. Our analysis also raises the interesting possibility that heat shrinking polymers such as SU-8 which support up to 7% strain may be better stress layer materials than vacuum deposited metals.

Future work will include modeling more complex hinge structures and comparing the analytical model to a finite-element model. The analytical model will be solved for several new cases to determine the effect on the curling and bending radius. These cases include:

1. Gradient stresses through the thickness of the stress metal layer.
2. A lithographically patterned stress layer (for example, a grating of chromium strips).
3. An elastic-perfectly plastic or elastic-plastic material model for the structural layer.
4. Non-rectangular hinge geometries.
5. Corrugated (Fig. 2-6) and perforated hinge geometries.

5.2 Residual Stress Measurements and Analysis

Chapter 3 explains the origin of the residual stress in deposited thin films. The intrinsic stress depends on the microstructure of the film. Therefore, it varies depending on the deposition parameters and may be affected by any subsequent processing steps (for example, the nano-patterning or release step). In the NSL evaporator, we found that it was possible to control the residual stress to within $\pm 10\%$ and that the stress decreased with increasing film thickness. The magnitude of the residual stress ranged from 1-2GPa. In addition to the strain from deposition, thermal strains may also arise due to ambient temperature fluctuations. Section 3.1.2 shows that these strains may alter the bending radius by 4% or more.

These findings yield two conclusions. First, the fold angle can be controlled to within $\pm 10\%$ which makes stress-actuated folding an excellent coarse positioning technique. We may intentionally create thermal strains (by laser heating, for example) to finely adjust the fold angle. However, during normal device operation ambient temperature changes will cause unwanted thermal strains that will affect the folded

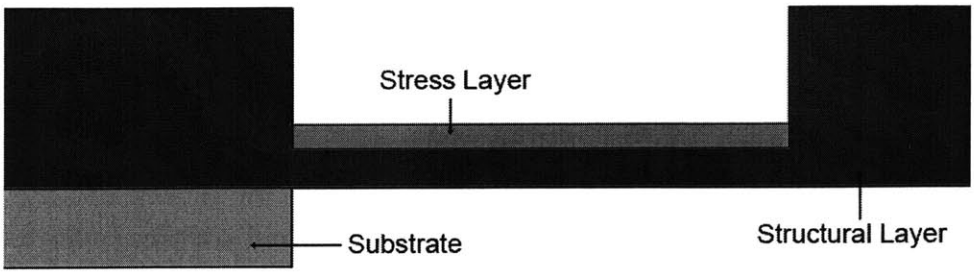

Figure 5-1: This thin hinge design maximizes the chromium residual stress, minimizes the bending radius, and maximizes the structural strength of the folded membrane.

structure. Therefore a latching technique is required to hold the folded membranes in place.

Second, it is desirable to use the thinnest chromium stress layer possible because the residual stress increases as the film thickness decreases. At the same time, we are constrained by Eq. 2.12 and need to thin the structural layer in proportion to the stress layer in order to still achieve the minimum bending radius. However, if the structural layer is too thin, the folded membrane may fracture or deform due to structural weakness. Therefore, we propose the hinge design shown in Fig. 5-1 in which the folded membrane may be more than 1μm thick and the hinge may be less than 50nm thick.

5.3 The Nanostructured Origami Process

The stress-actuated folding experimental results of Section 4.2 demonstrate the utility of the process. We were able to demonstrate the following:

1. Large silicon nitride membranes folded to angles proportional to the length of the chromium hinge (Fig. 4-5).

2. Single folds to precisely 45°, 90°, 180° and other angles (Figs. 4-5 and 4-6).

3. Multiple folds on a single membrane (Fig. 4-8).

4. Folding a corner cube (Fig. 4-11).

The highlight of the thesis is the demonstration of folded, nano-patterned membranes (Figs. 4-15, 4-16 and 4-18).

However, the current fabrication process is rudimentary and needs refinement. Listed below are four aspects that will be addressed in future experimentation.

1. A dry release process needs to be developed to avoid stiction (refer to Section 4.2.3) and to be more etch selective to allow the membranes to be patterned with deposited material. We will experiment with an HF vapor etch of a sacrifical SiO_2 layer to achieve this.

2. Compressive stress folds must be demonstrated to work in combination with the tensile stress folds. We will experiment with sputtered chromium to achieve compressive stress.

3. The hinge structure needs to be optimized for maximum strength and minimum bending radius. We will experiment with the corrugated hinge design of Fig. 2-6 and the thin hinge design of Fig. 5-1. It will be interesting to see how thin the hinge can be made and still remain strong enough to fold the attached membrane.

4. Stress-actuated folding needs to be characterized for different materials. It will be an important demonstration to show that we can fold silicon membranes. For the stress layer, we will experiment with tungsten and SU-8 (refer to Sections 2.3 and 3.1).

5.4 Additional Future Work

In addition to the already suggested experiments, future work in several other areas is required. This thesis has presented a viable method for folding nano-patterned membranes; however, Nanostructured Origami will also require a complementary alignment and latching scheme. To achieve fine alignment, we are experimenting with nano-magnets. The magnets can be positioned on the membranes and the substrate

so that after a 180° fold, they will approximately line up. Before folding, they are all magnetized in the same direction. After folding, the polarization of the membrane's magnets and the substrate's magnets will be reversed, causing them to attract and naturally align. To latch the membranes after they are folded and aligned, we are experimenting with pads of low-melting point material that can be annealed together. Photoresists and solder are two possible materials of choice.

As we experiment with more complicated devices which use both tensile and compressive stress folds, time sequencing of the folds will become necessary. This may be accomplished by patterning photoresist over the hinges to prevent them from actuating immediately upon release. The hinges can then be individually actuated by selectively removing the photoresist. If several different photoresists are used that are etch selective against each other, they could be removed sequentially to actuate the hinges in groups. For even better control, the photoresist could be melted off individual hinges by controlled laser heating.

Most importantly, we must demonstrate that Nanostructured Origami can be used to fabricate a useful structure. The simplest initial application is a multi-layered stack of diffractive optical elements, for example a 3-D Fresnel zone plate (refer to Section 1.2). Even with only tensile stress folds and relying on stiction forces to latch the membranes together, we may be able to create a five-layer diffractive structure by folding four membranes 180° back onto the substrate.

Appendix A

Melting Points of Common Metals

Table A.1: Melting Points of Common Metals

Element	**Melting Point, T_M (°K)**		T/T_M, at $T = 293$°K
Pb	598	[25]	0.49
Sb	903	[25]	0.32
Al	933	[25]	0.31
Au	1336	[25]	0.22
Cu	1356	[25]	0.22
Ni	1726	[25]	0.17
Fe	1807	[25]	0.16
Ti	1941	[35]	0.15
Pt	2041	[35]	0.14
Cr	2148	[25]	0.14
Re	2237	[35]	0.13
Nb	2750	[35]	0.11
Mo	2896	[35]	0.10
Ta	3290	[35]	0.09
W	3683	[25]	0.08

Appendix B

Photolithography Masks

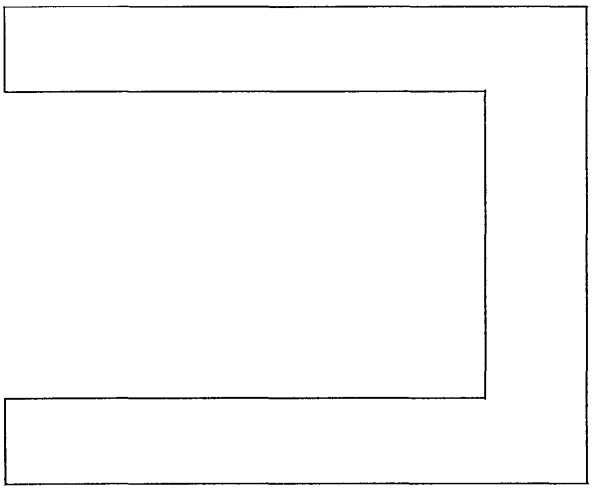

Figure B-1: Mask used in Experiment 4.1 to form the cantilevers. The bounded shape was etched away to form a cantilever.

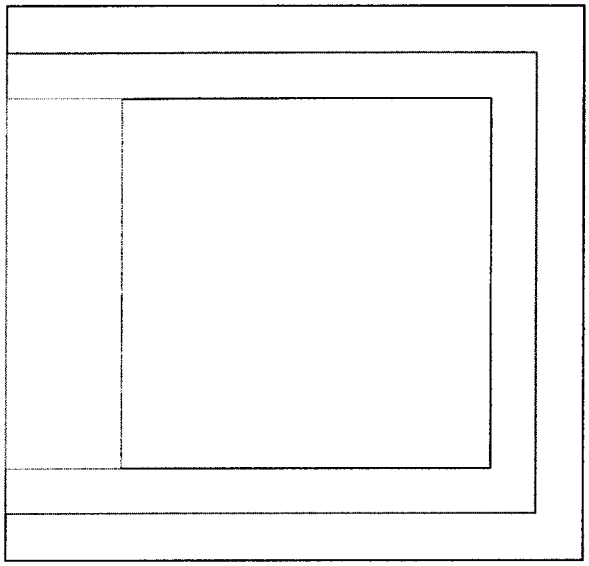

Figure B-2: Mask set used to create a single fold device in Experiment 4.2. The area bounded by the black layer is forms the cantilever, the area bounded by the red layer is the release pad (used in Experiment 4.2.5), and the area bounded by the green layer forms the stresses chromium hinge. The length of the hinge is 50μm and the length of the cantilever is 250μm.

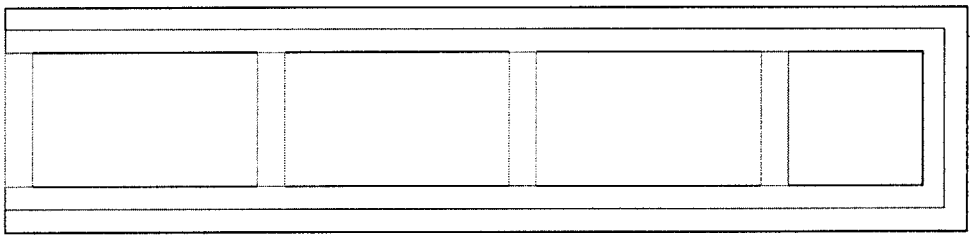

Figure B-3: Mask set used to create a multiple (four) fold device in Experiment 4.2. The area bounded by the black layer is forms the cantilever, the area bounded by the red layer is the release pad (used in Experiment 4.2.5), and the area bounded by the green layer forms the stresses chromium hinge. The length of each hinge is 30μm and the length of the entire cantilever is 1050μm.

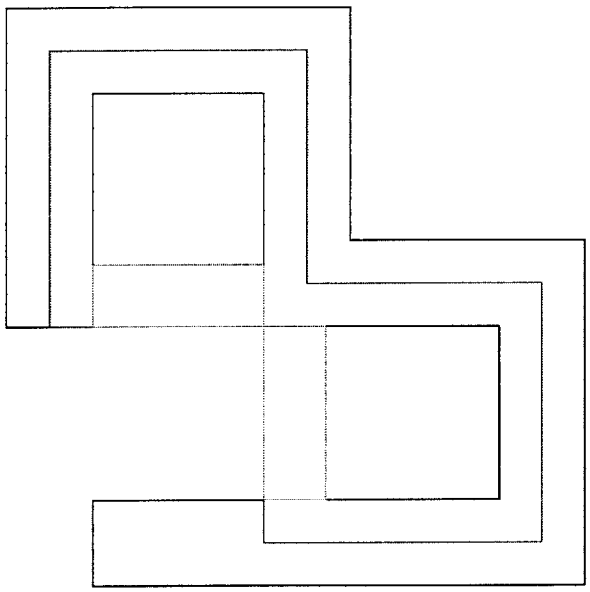

Figure B-4: Mask set used to create a corner cube device in Experiment 4.2. The area bounded by the black layer is forms the cantilever, the area bounded by the red layer is the release pad (used in Experiment 4.2.5), and the area bounded by the green layer forms the stresses chromium hinge. The length of each hinge is 37μm and the length of each cantilever is 143μm.

Bibliography

[1] M. H. Qi et al. A three-dimensional optical photonic crystal with designed point defects. *Nature*, 429(6991):538, 2004.

[2] D. Gil et al. Fabrication of high-numerical-aperture phase zone plates with a single lithography exposure and no etching. *J Vac Sci Technol B*, 21(6):2956, 2003.

[3] D. Gil et al. Parallel maskless optical lithography for prototyping, low-volume production, and research. *J Vac Sci Technol B*, 20(6):2597, 2002.

[4] E. E. Moon et al. Interferometric-spatial-phase imaging for six-axis mask control. *J Vac Sci Technol B*, 21(6):3112, 2003.

[5] A. Vorob'ev et al. Array of micromachined components fabricated using "micro-origami" method. *Jpn J Appl Phys 1*, 42(6B):4024, 2003.

[6] P. O. Vaccaro et al. Valley-fold and mountain-fold in the micro-origami technique. *Microelectr J*, 34(5-8):447, 2003.

[7] T. Tokuda et al. Fabrication and current-drive of sige/si 'micro-origami' epitaxial mems device on soi substrate. *Electron Lett*, 40(21):1333, 2004.

[8] M. Grundmann. Nanoscroll formation from strained layer heterostructures. *Appl Phys Lett*, 83(12):2444, 2003.

[9] W. J. Arora et al. Nanostructured origami 3d fabrication and assembly process using strain actuated folding. In *The 2nd International Symposium on Nanomanufacturing*, page 18, Daejeon, Korea, 2004.

[10] O. Schumacher et al. Lithographically defined metal-semiconductor-hybrid nanoscrolls. *Appl Phys Lett*, 86(14), 2005.

[11] C. L. Chua et al. Out-of-plane high-q inductors on low-resistance silicon. *J Microelectromech S*, 12(6):989, 2003.

[12] O. G. Schmidt et al. Semiconductor tubes, rods and rings of nanometer and micrometer dimension. *Physica E*, 13(2-4):969, 2002.

[13] H. Wu et al. Fabrication of topologically complex three-dimensional microstructures: Metallic microknots. *J Am Chem Soc*, 122(51):12691, 2000.

[14] J. Zou et al. Plastic deformation magnetic assembly (pdma) of out-of-plane microstructures: Technology and application. *Microelectromechanical Systems, Journal of*, 10(2):302, 2001.

[15] H. J. In et al. The nanostructured origami 3d fabrication and assembly process for nanomanufacturing. In *Nanotechnology, 2004. 4th IEEE Conference on*, page 358, 2004.

[16] M. Boncheva et al. Magnetic self-assembly of three-dimensional surfaces from planar sheets. *P Natl Acad Sci USA*, 102(11):3924, 2005.

[17] E. Shimada et al. Prototyping millirobots using dextrous microassembly and folding. In *Proc. ASME IMECE/DSCD*, 2000.

[18] L. X. Zhou et al. Corner-cube retroreflectors based on structure-assisted assembly for free-space optical communication. *J Microelectromech S*, 12(3):233, 2003.

[19] M. Horie et al. Micro-hinges changed flexural rigidity intermittently for micromechanism joints. *Microsyst Technol*, 9(6-7):381, 2003.

[20] A. Friedberger et al. Improved surface-micromachined hinges for fold-out structures. *J Microelectromech S*, 7(3):315, 1998.

[21] R. R. A. Syms et al. Surface tension-powered self-assembly of micro structures - the state-of-the-art. *J Microelectromech S*, 12(4):387, 2003.

[22] T. Ebefors et al. New small radius joints based on thermal shrinkage of polyimide in v-grooves for robust self-assembly 3d microstructures. *J Micromech Microeng*, 8(3):188, 1998.

[23] A. K. Sinha et al. Control of resistivity, microstructure, and stress in electron-beam evaporated tungsten films. *J Vac Sci Technol*, 10(3):436, 1973.

[24] R. Abermann et al. Internal-stress and structure of evaporated chromium and mgf2 films and their dependence on substrate-temperature. *Thin Solid Films*, 115(3):185, 1984.

[25] J. A. Thornton et al. Stress-related effects in thin-films. *Thin Solid Films*, 171(1):5, 1989.

[26] G. Thurner et al. Internal-stress and structure of ultrahigh-vacuum evaporated chromium and iron films and their dependence on substrate-temperature and oxygen partial-pressure during deposition. *Thin Solid Films*, 192(2):277, 1990.

[27] J. A. Thornton et al. Internal-stresses in metallic-films deposited by cylindrical magnetron sputtering. *Thin Solid Films*, 64(1):111, 1979.

[28] D. W. Hoffman et al. Internal-stresses in cr, mo, ta, and pt films deposited by sputtering from a planar magnetron source. *J Vac Sci Technol*, 20(3):355, 1982.

[29] R. O. E. Vijgen et al. Mechanical measurement of the residual stress in thin pvd films. *Thin Solid Films*, 270(1-2):264, 1995.

[30] F. Elstner et al. Comparative study of the stress in chromium films deposited by vacuum arc evaporation, vacuum evaporation, and dc magnetron sputtering. *Phys Status Solidi A*, 154(2):669, 1996.

[31] M. Mondol et al. Uniform-stress tungsten on x-ray mask membranes via he-backside temperature homogenization. *J Vac Sci Technol B*, 12(6):4024, 1994.

[32] P. O. Vaccaro et al. Strain-driven self-positioning of micromachined structures. *Appl Phys Lett*, 78(19):2852, 2001.

[33] B. Stark, editor. *Mems Reliability Assurance Guidelines for Space Applications*, volume 99-1. NASA JPL, Pasadena, CA, 1999.

[34] In *MEMS Workshop*, page 174, Napa Valley, CA, 1990.

[35] M. Winter. Webelements periodic table. *http://www.webelements.com*, 2005.

[36] G. P. Nikishkov. Curvature estimation for multilayer hinged structures with initial strains. *J Appl Phys*, 94(8):5333, 2003.

[37] J. Cybulski. *Modeling and Fabrication of Self-Assembling Micron-Scale Rollup Structures.* Master of science, MIT, 2004.

[38] Y. C. Tsui et al. An analytical model for predicting residual stresses in progressively deposited coatings .1. planar geometry. *Thin Solid Films*, 306(1):23, 1997.

[39] S. Morohashi et al. Characteristics of superconducting nb layer fabricated using high-vacuum electron beam evaporation. *Jpn J Appl Phys 1*, 40(2A):576, 2001.

[40] C. H. Chang. *Fabrication of Extremely Smooth Blazed Diffraction Gratings.* Master of science, MIT, 2004.

[41] W. M. van Spengen et al. A physical model to predict stiction in mems. *J Micromech Microeng*, 12(5):702, 2002.

[42] T. A. Savas et al. Properties of large-area nanomagnet arrays with 100 nm period made by interferometric lithography. *J Appl Phys*, 85(8):6160, 1999.